HADRONIC DECAYS OF THE D_S MESON AND A MODEL-INDEPENDENT DETERMINATION OF THE BRANCHING FRACTION FOR THE D_S DECAY TO PHI PI

A DISSERTATION
SUBMITTED TO THE DEPARTMENT OF PHYSICS
AND THE COMMITTEE ON GRADUATE STUDIES
OF STANFORD UNIVERSITY
IN PARTIAL FULFILLMENT OF THE REQUIREMENTS
FOR THE DEGREE OF
DOCTOR OF PHILOSOPHY

By
John Nicholas Synodinos
July 1995

To the memory of my parents,

Alexander and Chryssoula Synodinos

Abstract

During the running periods of the years 1992, 1993, 1994 the BES experiment at the Beijing Electron Positron Collider (BEPC) collected $22.9 \pm 0.7 pb^{-1}$ of data at an energy of 4.03 GeV, which corresponds to a local peak for $e^+ e^- \to D_s^+ D_s^-$ production. Four D_s hadronic decay modes were tagged:

- $D_s \to \phi \pi; \ \phi \to K^+ K^-$

- $D_s \to \overline{K^*}(892)^0 K; \ \overline{K^*}^0(892) \to K^- \pi^+$

- $D_s \to \overline{K^0} K; \ \overline{K^0_s} \to \pi^+ \pi^-$

- $D_s \to \overline{K^*}(892)^0 K^*; \ \overline{K^*}^0(892) \to K^- \pi^+; \ K^*(892) \to K^0 \pi^+; \ K^0_s \to \pi^+ \pi^-$

Using the method of double-tagging, BES performed the first model-independent measurement of $Br_{D_s \to \phi \pi}$. Our result was:

$$Br_{D_s \to \phi \pi} = 3.4^{+4.8+1.3}_{-1.7-0.7}$$

Acknowledgements

This work would not have been possible without the continuing guidance and support from BES collaborators, fellow graduate students, family members and friends. It is difficult to give proper recognition to all of them, and I wish to apologize up front to anyone whose contributions I have overlooked in these acknowledgements.

I owe many thanks to my advisor, Jonathan Dorfan, for providing me with guidance and encouragement. It was a priviledge to have been his graduate student. I wish to thank Bill Dunwoodie for his day to day advice. His understanding of physics and his willingness to share his knowledge have been essential to the completion of this analysis. Ralph Becker, Eric Soderstrom, Steve Schaffner and Colin Jessop, my next-door-office mates, very often went beyond the call of duty to answer questions and help. I would also like to thank the other graduate students in the BES experiment. They could always be counted on for a beer and some good chat after the BES collaboration meetings.

Christina Papageorgopoulos has provided me with patience, generosity and love. Her presence alone was an inspiration. My family has given me unwavering support over the years, through studies, work and personal hardship. My parents, Alexander and Chryssoula Synodinos, always taught me to enjoy life and to believe in myself. They were truly the ones that made it all possible, and it is to their memory that I am dedicating this thesis.

Contents

List of Tables

List of Figures

Chapter 1

Introduction and Motivation for Analysis

1.1 The Standard Model

The Standard Model of Particle Physics is man's most organized and thorough attempt to answer the question "What is the Universe made of?", and it constitutes one of the greatest scientific achievements of the twentieth century. With inputs from experiment, principle and phenomenology, it has identified the elementary building blocks of matter, and has analyzed the ways they interact with each other.

According to the Standard Model, all matter is made up of 12 elementary constituents:

- Six quarks : Up (u), Down (d), Strange, (s) Charm (c), Bottom (b), and Top (t)

- Six leptons: electron (e), muon (μ), tau (τ) and their respective neutrinos ν_e, ν_μ, ν_τ

Another class of particles, the "mediators" are the carriers of the forces responsible for the interactions between the constituents. These mediators are the photon (γ), the bosons W^+, W^-, Z^0, and the 8 gluons.

All particles interact with each other through the four known forces: Gravity, electromagnetic interaction, weak interaction and strong interaction. *Gravity* is not treated in the Standard model, partly because its effects are negligible in the atomic scale. The *electromagnetic interaction* is mediated by the photon γ, and is responsible for light and the full spectrum of electromagnetic waves, as well as for most of the chemical structure of the matter around us. The photon is massless, (which accounts for the electromagnetic interactions' infinite range), and couples to the particles' charge. The electromagnetic coupling constant (also known as the "fine structure constant") is denoted by $\alpha \equiv e^2/(4\pi\hbar c)$ and, for low energies, it is equal to 1/137. The *weak interaction* is mediated by the $W^\pm$ and Z^0 bosons, and is the force governing, among other phenomena, nuclear β-decay and neutrino interactions. It is a very short range force (10^{-2} fermi), due to the massive nature of its mediating bosons. In the energy range of the measurements described in this thesis, the weak coupling α_W is only 10^{-3} of the electromagnetic coupling (hence the characterization "weak"), but it is still 10^{40} times stronger than gravity. The weak and electromagnetic interactions have been unified into the $SU(2) \times U(1)$ structure of the *electroweak* interaction. It is with respect to this structure that we separate the quarks and leptons into six "weak isospin" doublets:

$$\begin{pmatrix} d \\ u \end{pmatrix} \qquad \begin{pmatrix} c \\ s \end{pmatrix} \qquad \begin{pmatrix} b \\ t \end{pmatrix} \qquad \begin{pmatrix} e \\ \nu_e \end{pmatrix} \qquad \begin{pmatrix} \mu \\ \nu_\mu \end{pmatrix} \qquad \begin{pmatrix} \tau \\ \nu_\tau \end{pmatrix}$$

The *strong interaction* holds the quarks together into bound states, and has a range of ~ 1 fermi (comparable to the dimensions of the atomic nucleus). It is mediated by 8 gluons, corresponding to the 8 members of the irreducible representation of $SU(3)$ of color. (Color, which comes in 3 states – usually referred to as "red", "blue" and "green", is the analogous of charge in the strong interactions). In the energy range of our measurements, the strong coupling constant α_s has a value of ~ 1, or 10^2 times stronger than the elecromagnetic coupling.

Individual quarks have never been observed in a free state. Instead, they form bound states called mesons (consisting of a quark-antiquark pair) or baryons (consisting of three quarks or three antiquarks). Both mesons and baryons are collectively known as hadrons. Even though all quarks have fractional charges, their observable

combinations always have integral charge. Also, quarks of different colors combine in such a way that mesons and baryons are colorless.

Embedded in the Standard Model is a set of conservation laws: Conservation of energy and momentum carries over directly from classical physics, as a result of the time and space invariance of the Lagrangian. Conservation of charge is a result of the gauge invariance of Quantum Electrodynamics (QED). Conservation of baryon number and lepton number (within each lepton family independently) has always been observed, yet the Standard Model offers no compelling reason why it should be so. Finally, Charm, Strangeness, Isospin, parity and charge conjugation are conserved in the stong and electromagnetic interactions, but violated in the weak ones.

One should not think of the Standard Model as the work of any one individual. Rather, it is the result of the efforts of many physicists, who worked for a generation, trying to order the multitude of the hadrons discovered using ever expanding concepts of summetry. To explain the abnormally long lifetime of the Λ - hyperon, Gell-Mann [1] and Nishijima [2] independently proposed the existence of a new, additive quantum number, "strangeness". This led to the $SU(3)$ classification of the then-known hadrons, according to their "flavor" content (u,d,and s). We now know this $SU(3)$ of flavor to hold only approximately, because of the mass difference between the s, the u and the d quarks. In 1964, Gell-Mann [3] came up with the theory that the u, s and d "flavors" were not just mathematical constructs, but actual physical particles – he called them quarks. About the same time, Glashow [4], Weinberg [5] and Salam [6] unified QED and the weak interactions in a $SU(2) \times U(1)$ electroweak theory for leptons, which couples the γ and the Z^0 through the Weinberg angle θ_W. To extend the electroweak theory to quarks, Glashow, Iliopoulos and Maiani [7] proposed the existence of a fourth quark, the "charm", which was actually discovered at SLAC [8] and Brookehaven [9] in 1974.

Despite the Standard Model's spectacular success at explaining the fundamental structure of matter, most physicists concede that it may not be the ultimate theory of the Universe. For one, the number of arbitrary parameters ranges from 18 to 25, depending on whether one stipulates massless or massive neutrinos. In addition, the Standard Model offers no explanation for the mass, number and classification

of the elementary particles, or for the baryon and lepton number conservation laws. Also, the four interactions are more or less distinct, and Gravity is, to some level, incompatible with the mathematical structure of the other three. The far - reaching goal of theoretical physics, however, is to unify the four forces in a single set of equations, much like Maxwell did with Electricity and Magnetism. This unification will presumably occur in such a way that at very high energies (of the order of the Plank scale, or $\sim 10^{15}$ GeV) all coupling constants attain equal values, and the apparently separate interactions merge. At present, only a unification of the weak and electromagnetic forces into the electroweak interaction has had any significant success; the quest goes on.

1.2 Weak Interactions – the K-M Matrix

Historically, the first form of a weak coupling came from Fermi [10] in an attempt to explain the radiative β-decay. He stipulated a current-current interaction of zero range, and of a strength determined by a coupling constant G, with dimensions of GeV^{-2}. The matrix element was given by

$$M = G(\overline{u}_n \gamma^\mu u_p)(\overline{u}_{\nu_e} \gamma_\mu u_e)$$

Here u_i signifies the free Dirac spinor solution for the fermion i, and the γ's are the Dirac matrices. In the standard (Pauli - Dirac) representations, these matrices have the form

$$\gamma^0 = \begin{pmatrix} I & 0 \\ 0 & -I \end{pmatrix} \qquad \gamma^i = \begin{pmatrix} 0 & \sigma^{(i)} \\ -\sigma^{(i)} & 0 \end{pmatrix}, \qquad i = 1,2,3$$

and

$$\gamma^5 \equiv i\gamma^0\gamma^1\gamma^2\gamma^3 = \begin{pmatrix} 0 & I \\ I & 0 \end{pmatrix}$$

where $\sigma^{(i)}$ is the ith Pauli spin matrix.

Fermi's formulation is of mostly historical interest (note the absence of a propagator), but it was the first attempt to extend the language of the Dirac equation beyond the well understood Electromagnetic domain. Now we know the weak interactions
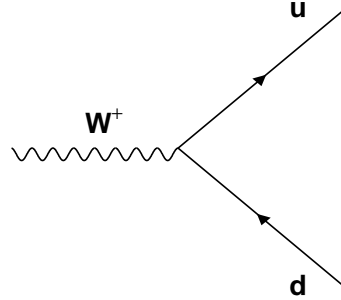
Figure 1.1: The charge raising weak current

to proceed through massive vector bosons, in what is known as the V-A (Vector - Axial Vector) coupling: The charge raising weak current of Fig. 1.1 corresponds to the notation

$$J_q^\mu = \overline{u}_u \gamma^\mu \frac{1}{2}(1 - \gamma^5)u_d$$

in accord with the fact that the W-propagator couples only to left-handed fermion doublets. The neutral currens, on the other hand, are written as

$$J_q^\mu \propto \overline{u}_i \gamma^\mu \frac{1}{2}(c_V^i - c_A^i \gamma^5)u_i$$

where the index i refers to the particle type. Neutrinos are left-handed, and $c_V^\nu = c_A^\nu = 1/2$. For quarks and massive fermions, though, $c_V \neq c_A$, and we can have (small) right-handed conributions. Flavor changing neutral currents are not allowed in the theory, and have never been observed in experiment.

The weak current can also couple quarks that belong to different generations (as in the case of $K^+ \to \mu^+ \nu$). To account for this fact (while preserving the weak coupling universality) Cabibbo [11] introduced the notion that the W - propagator does not couple to the mass eigenstates of the different quarks, but to a slightly "mixed" weak eigenstate doublet:

$$\begin{pmatrix} u \\ d \end{pmatrix} \to \begin{pmatrix} u \\ d' \end{pmatrix} \qquad d' = d\cos\theta_C + s\sin\theta_C$$

In the 4-quark model, then, a W - vertex would preferably couple a u to a d and a c to an s, yet a (much weaker) cross-coupling could still occur.

$$J^\mu = \begin{pmatrix} \overline{u} & \overline{c} \end{pmatrix} \frac{\gamma^\mu (1 - \gamma^5)}{2} \begin{pmatrix} \cos\theta_C & \sin\theta_C \\ -\sin\theta_C & \cos\theta_C \end{pmatrix} \begin{pmatrix} d \\ s \end{pmatrix}$$

Measuring the ratio

$$\frac{\Gamma(K^+ \rightarrow \mu^+ \nu_\mu)}{\Gamma(\pi^+ \rightarrow \mu^+ \nu_\mu)} \sim \sin^2\theta_C$$

we get a value for θ_C about 13 degerees.

In the 6 quark model, the weak current is of the form:

$$\begin{pmatrix} \overline{u} & \overline{c} & \overline{t} \end{pmatrix} \frac{\gamma^\mu (1 - \gamma^5)}{2} \begin{pmatrix} M_{KM} \end{pmatrix} \begin{pmatrix} d \\ s \\ b \end{pmatrix}$$

where the Cabibbo matrix generalizes into the Kobayashi-Maskawa matrix M_{KM} [12]:

$$M_{KM} = \begin{pmatrix} V_{ud} & V_{us} & V_{ub} \\ V_{cd} & V_{cs} & V_{cb} \\ V_{td} & V_{ts} & V_{tb} \end{pmatrix}$$

The diagonal elements have a magnitude close to 1, and correspond to the mixing within the three quark generations. The off-diagonal elements are of smaller magnitude (typically 0.0 - 0.2) and correspond to inter-generational mixing. All entries are complex numbers, so, in general, we could have as many as 18 separate parameters in the matrix. After we impose the requirements of unitarity (to ensure conservation of probability for the quark current), and redefine the quark wavefunctions to absorb all allowable phases, we can express the KM matrix in terms of four fundamental parameters: θ_{12}, θ_{13}, θ_{23} (the inter-generation mixing angles) and the complex phase δ. The standard parametrization of the KM matrix becomes:

$$\begin{pmatrix} c_{12}c_{13} & s_{12}c_{13} & s_{13}e^{-i\delta} \\ -s_{12}c_{23} - c_{12}s_{23}s_{13}e^{-i\delta} & c_{12}c_{23} - s_{12}s_{23}s_{13}e^{-i\delta} & s_{23}c_{13} \\ s_{12}s_{23} - c_{12}c_{23}s_{13}e^{-i\delta} & -c_{12}s_{23} - s_{12}c_{23}s_{13}e^{-i\delta} & c_{23}c_{13} \end{pmatrix}$$

where c_{ij} (s_{ij}) is the cosine (sine) of θ_{ij}. The complex phase δ is presumably related to the $C - P$ violating nature of the weak interactions, and is a topic of current interest and research.
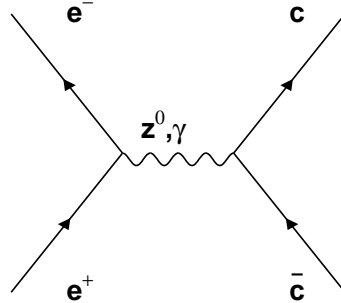
Figure 1.2: First order diagram for $e^+ e^- \to c\bar{c}$

1.3 Charm Production in $e^+ e^-$ Colisions

Since electrons and quarks couple both to photons and to the massive weak bosons, quark creation in $e^+ e^-$ collisions can proceed via electromagnetic and weak contributions, as shown in Fig. 1.2. In the τ - charm energy region (3.5 - 4.5 GeV), the relative strength of the weak compared to the electromagnetic sector is of the order of 10^{-4}, so we can safely assume that the $q\bar{q}$ procduction is proceeding mainly through a single photon exchange.

If f^+, f^- are fermions other than electrons (e.g. muons), then the formula for inelastic scattering $e^+ e^- \to f^+ f^-$, is given by

$$\sigma_{e^+ e^- \to \mu^+ \mu^-} = \frac{4\pi \alpha^3}{3s}$$

where α is the fine structure constant $e^2/4\pi$ ($\sim 1/137$) and $\sqrt{s}$ is the center of momentum energy. If we take into account the color and flavor multiplicity of quarks, and ignore quark mass differences, final state radiation and QCD corrections, we get a cross-section for the process $e^+ e^- \to$ (hadrons) given by

$$\sigma_{e^+ e^- \to hadrons} = 3 \sum_q e_q^2 \left(\sigma_{e^+ e^- \to \mu^+ \mu^-} \right)$$
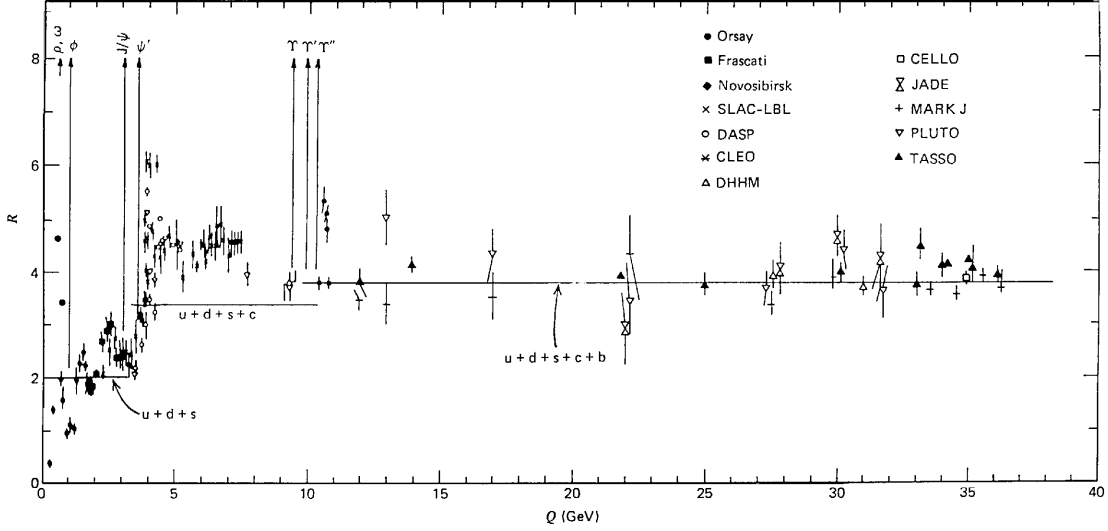
Figure 1.3: R as a function of energy (from Halzen & Martin, *Quarks and Leptons*, John Wiley & Sons , 1984)

which implies that

$$R \equiv \frac{\sigma_{e^+e^-\rightarrow hadrons}}{\sigma_{e^+e^-\rightarrow\mu^+\mu^-}} = 3\sum_q e_q^2$$

This formula predicts steps in R at the energies that correspond to the the masses of $c\bar{c}$ and $b\bar{b}$ subsystems. This is generally true, if the energy is far from resonances. In the region between 3.8 and 4.5 GeV, however, a complicated energy dependence for R is observed, largely due to the resonant structure of the $c\bar{c}$ system (see Fig. 1.3).

The "coupled-channel model" of Eihcten *et al.* [13] attempts to predict several charmed meson production cross sections, by using the detailed input of the $c\bar{c}$ spectroscopy. It assumes a quark potential of the form:

$$V(r) = -\frac{4\alpha_s}{3r} + \frac{r}{A^2}$$

where r is the quark - antiquark separation and α_s the strong coupling constant. The potential bears no explicit dependence on the quark flavors, and any implicit dependence has to do with differences in the quark masses. In the model, then, we

Coupled Channel Model
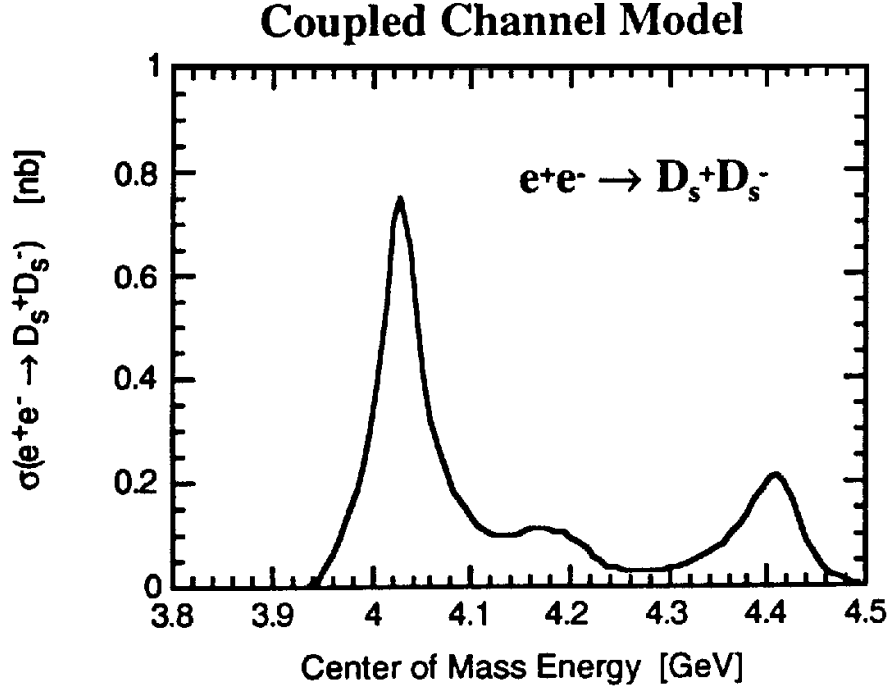
Figure 1.4: The $e^+e^- \to D_s^+ D_s^-$ cross-section as a function of the energy in the BES energy region

assume that the same potential governs the dynamics of the $c\bar{c}$ bound system, as well as the decays into $c\bar{q}$ mesons (here q stands for u, d or s). Then the Hamiltonian becomes:

$$H = \int \rho_1(x)V(x-y)\rho_2(x)d^3x d^3y$$

and we can treat the $c\bar{q}$ meson fields as additional degrees of freedom of the $c\bar{c}$ system, with the $q\bar{q}$ pair described by the action of second- quantized creation and annihilation operators on the vacuum.

Using the Eichten model, together with the world average for quark and meson masses, Lockman [13] gives the production cross-sections for D_s shown in Fig. 1.4. For direct Ds pair production, the model predicts a peak at $\sqrt{s} = 4.03$ GeV, with a
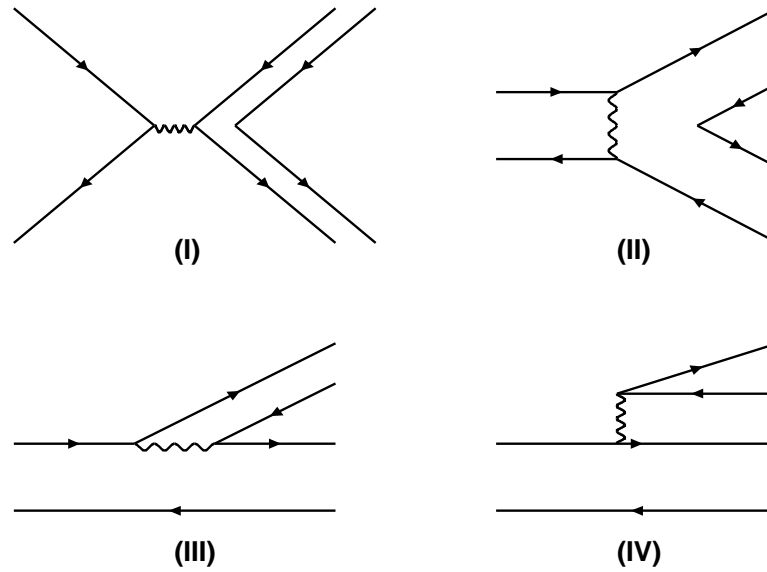
Figure 1.5: The four possible first order diagrams for D_s weak decay. (I): annihilation; (II): W exchange; (III): internal W emission; (IV): spectator decay

cross-section of 750 pb.

1.4 D_s decays

Charm and strangeness conservation forbid the D_s to decay via strong and electromagnetic interactions, so the D_s decomposition proceeds through the weak interaction. To lowest order in the weak coupling G_F, we can have contributions from four diagrams, shown in Fig. 1.5 Since the D_s's have spin 0, diagram (I) is helicity suppressed. Diagram (II) is Cabibo and color suppressed. Diagram (III) is also supressed because

of color matching, therefore the dominant decay diagram is (IV), the spectator decay. In this configuration, the heavy quark decays through a single W - exchange, with a first order (or "bare") Hamiltonian:

$$H^0 = \frac{G_F}{\sqrt{2}} V_{12} V_{34}^* (\overline{q_{2i}} \gamma^\mu (1 - \gamma_5) q_{1i})(\overline{q_{4i}} \gamma^\mu (1 - \gamma_5) q_{3i})$$

where i, j are color indeces, and the quark masses are assumed to be much smaller than the mass of the W.

We note that this is independent of the light quark flavor, and analogous to the Hamiltonian for the muon decay. Therefore, we would expect a simple scaling of the muon lifetime to give an identical lifetime for all the D - mesons (up to small corrections due to phase space and the K-M elements)

$$t_{D\pm} = t_{D^0} = t_{D_s} = \frac{5}{192} \frac{G_F^2 m_c^5}{\pi^3} \simeq 9 \times 10^{-13} sec$$

This is not the case. From MkIII we have:

$t_{D^0} = (4.21 \pm 0.10) \times 10^{-13} \text{sec}$

$t_{D\pm} : t_{D^0} : t_{D_s} = 2.5 : 1 : 1$

However, the semi-leptonic decay widths of the D and the D_0 mesons are roughly equal, so the differences in the lifetimes must be attributable to some exclusively hadronic effect.

QCD effects to lowest order in α_s can be represented by the following diagrams [14]
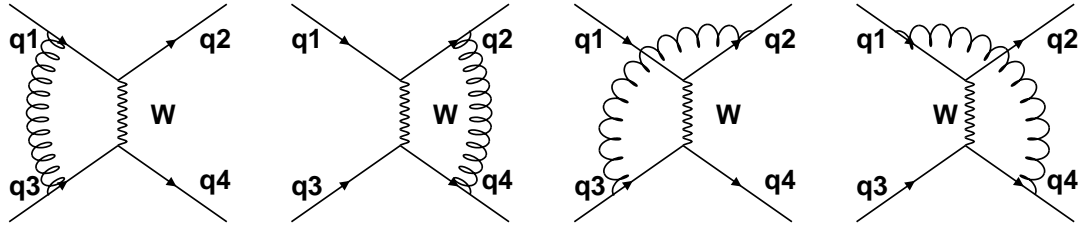
Now if we assume that all vertex and self-energy corrections have been absorbed into G_F we have, as a first-order correction on H^0,

$$H^1 = H^0 - \frac{G_F}{\sqrt{2}} \frac{3\alpha_s}{8\pi} \ln \frac{m_W^2}{\mu^2} V_{12} V_{34}^* (\overline{q_2} \lambda_i q_1)_L (\overline{q_4} \lambda_i q_3)_L$$

where μ is the charm quark mass, and we used the W mass m_W for the ultraviolet cutoff limit.

Making use of the Fiertz identity and employing some λ-algebra, we get:

$$H^1 = \frac{G_F}{\sqrt{2}} V_{12} V_{34}^* [(1 + \frac{\alpha_s}{4\pi} \ln \frac{m_W^2}{\mu^2})(\overline{q_2}q_1)_L(\overline{q_4}q_3)_L - \frac{3\alpha_s}{4} \ln \frac{m_W^2}{\mu^2}(\overline{q_2}q_3)_L(\overline{q_4}q_1)_L]$$

If we define

$$c^\pm = 1 \mp \frac{\alpha_s}{2\pi} \ln \frac{m_W^2}{\mu^2}$$

and

$$c_{1,2} = \frac{(c^+) \pm (c^-)}{2}$$

the Hamiltonian for the D mesons becomes

$$H^1 = \frac{G_F}{\sqrt{2}} V_{cs} V_{ud}^* [c_1(\overline{s}c)_L(\overline{u}d)_L + c_2(\overline{s}d)_L(\overline{u}c)_L]$$

The exact value of the $c^\pm$ coefficients depends on the value we choose for the running coupling constant α_s. For leading log calculations, and using again the charm quark mass as our characteristic mass scale, we get $c^+ \simeq 0.74$ and $c^- \simeq 1.18$. Now, in the limit that $c^- \gg c^+$, the Hamiltonian reduces to

$$H^1 = \frac{G_F}{\sqrt{2}} V_{cs} V_{ud}^* [(\overline{s}c)_L(\overline{u}d)_L - (\overline{s}d)_L(\overline{u}c)_L]$$

which vanishes for the D^+, but not for the other two D mesons. As $c^- > c^+$, we see that the hard gluon corrections already introduce a large destructive interference at the quark level, which is consistent with the long D^+ lifetime. This argues favorably for the validity of the model. In the next section, we can follow a use of this model, to arrive at predictions for D_s branching fractions.

1.5 BSW – the factorization approach

The process described in section 1.4 can get extermely complicated, as one tries to calculate hard and soft gluon corrections to higher and higher order. To sidestep this difficulty, many authors assume the effective Hamiltonian H^1 to describe the short distance effects sufficiently well, absorb all the long distance effects in the hadronization

process, and then use hadron (instead of quark) currents to calculate the transition matrix elements. This separation of long- and short- distance effects is called the "Factorization approach".

In the Bauer, Stech and Wirbel (BSW) model [15] the transition amplitude for the decay of a D meson into a 2-body state of vector and/or pseudoscalar mesons is given by

$$T_{(D \to f)} = \alpha_1 \langle f | (\overline{s}_L \gamma_\mu c_L)_H (\overline{u}_L \gamma_\mu d_L)_H | D \rangle + \alpha_2 \langle f | (\overline{u}_L \gamma_\mu c_L)_H (\overline{s}_L \gamma_\mu d_L)_H | D \rangle$$

where the subscript H indicates that the currents operate on hadron states, and the coefficients α are defined to be

$$\alpha_1 = \frac{1}{2}(c^+ + c^-) + \frac{\xi}{2}(c^+ - c^-)$$

and

$$\alpha_2 = \frac{1}{2}(c^+ - c^-) + \frac{\xi}{2}(c^+ + c^-)$$

ξ is a factor that describes the color suppression of internal vs. external W - emission. In principle, ξ should be close to $1/N$, (where N the number of colors), but in the model it is left as a free parameter, to account for hadronization and other long-distance effects.

BSW, then, make the factorization anzats:

$$\langle f | J_\mu J^\mu | D \rangle \simeq \langle X1, X2 | J_\mu | 0 \rangle \times \langle X1, X2 | J_\mu | D \rangle$$

or, for example,

$$\langle \overline{K^0} \pi^+ | H^1 | D^+ \rangle \propto \alpha_1 \langle \overline{K^0} | (\overline{s}c)_L | D \rangle \langle \overline{\pi^+} | (\overline{u}d)_L | 0 \rangle + \alpha_2 \langle \overline{K^0} | (\overline{s}d)_L | 0 \rangle \langle \overline{\pi^+} | (\overline{u}c)_L | D \rangle$$

We can now try to parametrize the matrix elements into a combination of form-factors, which will absorb the uncertainties of the spacial distribution of the hadrons and the hadronic current. Since the D mesons are pseudoscalars, we construct a general form of the matrix elements for the decays of the D into vectors (V) and/or pseudoscalars (P), with the right transformation properties and behavior at the free particle limit [16]:

$$\langle P | J_\mu | 0 \rangle = i f_P k_\mu \qquad\qquad \langle V | J_\mu | 0 \rangle = i f_V m_V \epsilon_\mu^V$$

$$\langle P|J_\mu|D\rangle = \left(k^D + k^P - \frac{m_D^2 - m_P^2}{q^2}q\right)_\mu F_1(q^2) + \frac{m_D^2 - m_P^2}{q^2}q_\mu F_0(q^2)$$

and

$$\langle V|J_\mu|D\rangle = \frac{2}{m_D + m_V}\epsilon_{\mu\alpha\beta\gamma}\epsilon_\alpha^V k_\beta^D k_\gamma U(q^2) + i\epsilon_\mu^V(m_D + m_V)A_1(q^2)$$

$$+i\frac{\epsilon^V \cdot q}{m_D + m_V}(k^D + k^V)_\mu A_2(q^2)$$

$$-2i\frac{\epsilon^V \cdot q}{q^2}m_V q_\mu[(A_3(q^2) - A_0(q^2))]$$

The quantity q is the four-momentum transfer $k^D - k^P$ (or $k^D - k^V$); ϵ^V denotes the spin vector of V, and f_P, f_V are the pseudoscalar and vector decay constants. The various form-factors are assumed to be dominated by the nearest pole:

$$F_i, A_i, V(q^2) \simeq \frac{h}{1 - q^2/m_D}$$

with h depending on the hadronic wavefunction overlap integral. In addition, the form-factors satisfy:

$$F1(0) = F_0(0)$$

$$A3(0) = A_0(0)$$

and

$$A_3(q^2) = \frac{m_D + m_V}{2m_V}A_1(q^2) - \frac{m_D - m_V}{2m_V}A_2(q^2)$$

Using the Mark III branching fractions for the D^0 and D decays [17], BSW find

$$\alpha_1 \simeq 1.2 \pm 0.1 \qquad \alpha_2 \simeq -0.5 \pm 0.1$$

Taking into account isospin amplitudes, and (higher order) weak annihilation diagrams, they arrive at a prediction for $D_s \to \phi\pi$ branching fraction:

$$Br_{D_s \to \phi\pi} = 2.8\%$$

1.6 D_s absolute branching fractions – motivation and method

From the previous sections it becomes apparent that a model-independent determination of the absolute D_s branching fractions (or, equivalently, the D_s production cross-section) will be a valuable test of both the factorization hypothesis and the coupled - channel model.

Up to now, no experiment has measured the absolute branching fractions of the D_s. All of the D_s branching ratios in the literature are quoted with respect to $Br_{Ds \to \phi\pi}$, this being a relatively abundant and background-free mode. To calculate $Br_{Ds \to \phi\pi}$, the various collaborations have generally used one of two different methods of approach, both of which are model-dependent and require theoretical input: In the first method, experiments would count the $D_s \to \phi\pi$ decays produced, and then make a (theoretical) estimate of the D_s pair production cross-section $R(D_s)$; this generally reduces to an estimate of the relative probability of an $s\bar{s}$ quark pair being produced out of the vacuum. This was the approach of HRS [18] TASSO [19] and CLEO(1989) [20]. In the second method, experiments would measure the ratio $Br_{D_s \to \phi\pi}/Br_{D_s \to \phi l \nu_l}$ and then assumme that

$$\frac{\Gamma(D_s^+ \to \phi l^+ \nu_l)}{\Gamma(D^+ \to K^{*0} l^+ \nu_l)} = \mathcal{F}_s$$

where $\mathcal{F}_s$ a model-dependent parameter with a value close to 1. Since $\Gamma(D^+ \to K^{*0} l^+ \nu_l)$ is known, the $D_s \to \phi\pi$ branching fraction can then be calculated in a straightforward way. This was the approach of NA14 [21], CLEO(1994) [22], ARGUS [23] and E687 [24]. In addition to these two methods, Muheim and Stone [25] employ a factorization anzats for the $B^0 \to D^* D_s^-$ two-body decays to estimate f_{D_s}, and then use experimental input for the ratio $\Gamma(D_s \to \mu\nu/\Gamma(D_s \to \phi\pi$ to calculate $Br_{D_s \to \phi\pi}$. A summary of all model-dependent calculations for $Br_{D_s \to \phi\pi}$ mentioned above is shown in Table 5.1.

In our experiment we used the double-tagging method to make a model-independent, direct measurement of the $Ds \to \phi\pi$ branching ratio. At $\sqrt{s} = 4.03\text{GeV}$, D_s are

COLLABORATION	YEAR [REF.]	model-dependent quantity	$Br_{D_s \to \phi\pi}$
Muheim	1994 [25]	f_{D_s}	$3.1 \pm 0.9\%$
Muheim	1994 [25]	$R(D_s)$	$4.6 \pm 1.5\%$
Muheim	1994 [25]	$\mathcal{F}_s$	$3.7 \pm 1.0\%$
CLEO	1994 [22]	$\mathcal{F}_s$	$5.1 \pm 0.4 \pm 0.4\%$
E687	1993 [24]	$\mathcal{F}_s$	$3.1 \pm 0.9 \pm 0.5\%$
ARGUS	1991 [23]	$\mathcal{F}_s$	$2.4 \pm 1.0\%$
NA14	1990 [21]	$R(D_s)$	$4.6 \pm 1.5\%$
CLEO	1989 [20]	$R(D_s)$	$2 \pm 1\%$
TASSO	1987 [19]	$R(D_s)$	$3.3 \pm 1.6 \pm 1.0\%$

Table 1.1: A summary of the model-dependent results for $Br_{D_s \to \phi\pi}$

produced directly in pairs, since the process $e^+ e^- \to D_s D_s^*$, $D_s^* \to D_s \gamma$ is not energetically allowed. Therefore, by comparing all the events in which both D_s have been tagged and fully reconstructed with the events in which only one of the D_s has been tagged and reconstructed, we can arrive at an estimate for the absolute D_s hadronic branching fraction. In more detail, if we attempt to tag n different decay modes, we have:

$$Br_{D_s \to \phi\pi} = 2 \cdot \frac{N_{DT}}{N_{ST}} \cdot \frac{\sum_i^n b_i \epsilon_i}{\sum_{i,j}^n b_i b_j \epsilon_{ij}}$$

where b_i and ϵ_i are the relative branching fraction $\Gamma_i / \Gamma_{\phi\pi}$ and the single tag detection efficiency of the ith mode, and ϵ_{ij} is the double tag detection efficiency for the final state i vs. j.

Mark III [26] used this method, investigating 28 double tag final states, without observing any candidates. They arrived at a 90% confidence level upper limit of

$$Br_{D_s \to \phi\pi} < 4.1\%$$

Chapter 2

Experimental Apparatus

2.1 The BEPC Storage Ring

The data used in this thesis were taken with the Beijing Spectrometrer (BES) detector at the Beijing Electron-Positron Collider (BEPC) storage ring [27] The BES collaboration is an ongoing, joint effort between the High Energy Physics communities in the United States and the People's Republic of China. The participants on the U.S. side are Boston University, CalTech, Colorado State University, MIT, SLAC, University of Hawaii, University of California at Irvine, University of Texas at Dallas, and University of Washington at Seattle. On the Chinese side, the main participant is the Institute of High Energy Physics (IHEP) in Beijing, PRC.

The BEPC facility is located on the campus of the IHEP, in the outskirts of Beijing, and it consists of three main subsystems: The BEPC collider, the BES magnetic spectrometer, and synchrotron a radiation facility.

Fig. 2.1 shows the layout of BEPC. Electrons first enter a 30 MeV pre-injector, and are then accelerated to 120 Mev in a linac. At the 150 MeV point, a tungsten target can be inserted for the production of positrons. After that, electrons and positrons get accelerated to 1.1 - 1.4 GeV, at which point they get injected in the storage ring. Inside the storage ring, the beams get an additional energy kick, to the operational value of 1.5 - 2.8 GeV/beam. The storage ring has a circumference of 240.4m, with two roughly semi-circular arcs, and two long straight sections. The BES detector is located
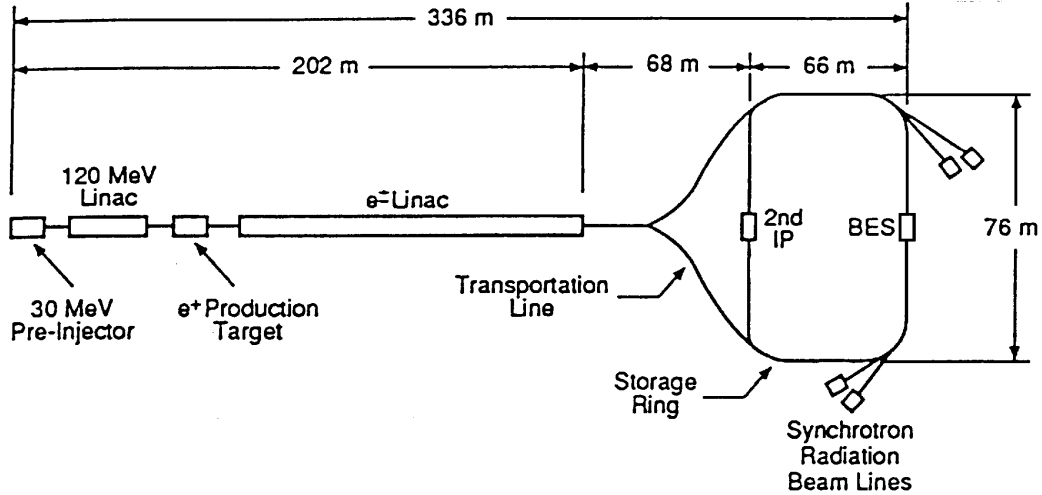
Figure 2.1: Schematic layout of BEPC

in the middle of one of these straight sections. There is space allocated for a second interaction point, but, at present, only the BES interaction region is operational. The maximum sustainable luminosity at $\sqrt{s} = 4GeV$ is $\sim 7.0 \times 10^{30}/cm^2/sec$, scaling linearly with $\sqrt{s}$. This corresponds to a circulation current of about 30 mA per beam. The total luminosity lifetime is 3 - 5 hours, depending on the beam energy.

2.2   The BES Spectrometer

The BES detector is a general purpose magnetic spectrometer, largely based on the design of the Mark III detector used at the SPEAR ring at SLAC. A layout of the detector can be seen in Fig. 2. From the interaction region outward, we can see the central drift chamber (CDC), the main drift chamber (MDC), the Time of Flight system, the shower counter system, the magnet coil, and, finally, the muon identifier.
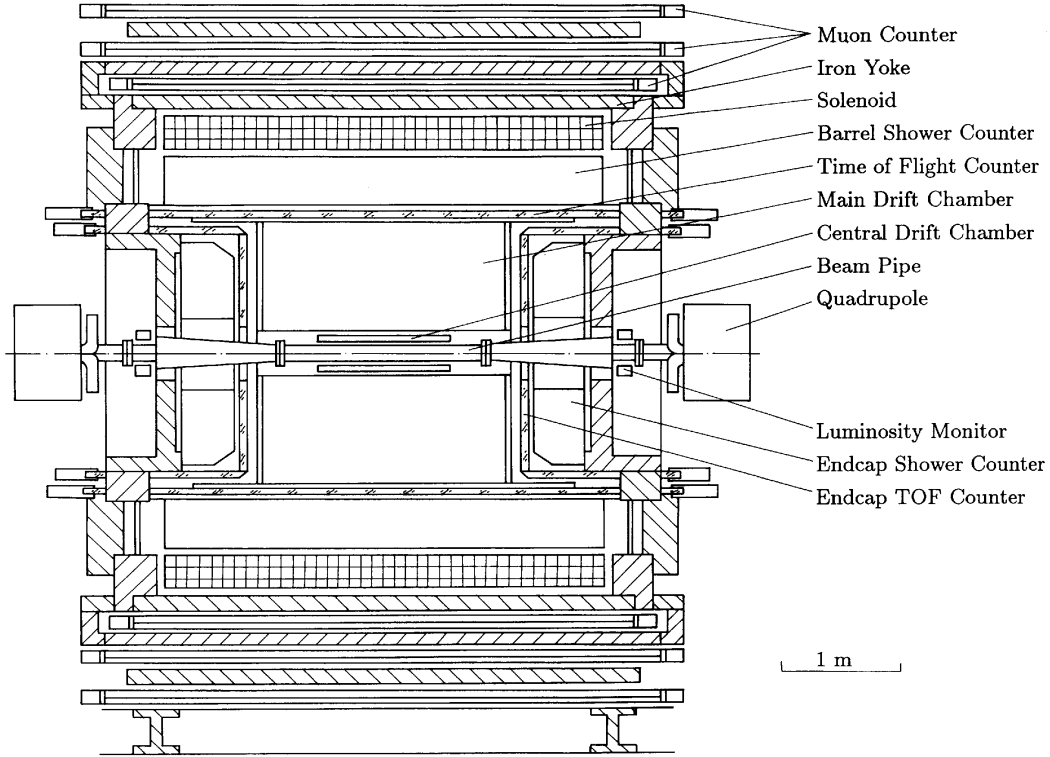
Figure 2.2: Cross-sectional diagram of BES

2.3   The BES Central Drift Chamber (CDC)

The Central Drift Chamber of BES is located between the beam pipe and the main drift chamber. It is cylindrical in structure, measuring 114cm (in length) × 30.2cm (in diameter). The solid angle coverage is 96% of 4π. To minimize multiple scattering, both the inner and the outer tubes are made of lightweight $1.55g/cm^3$ carbon fiber material. The tubes' thicknesses are 1mm and 2 mm, respectively. There are four layers of sense wires, each layer containing 48 wires; pairs of field wires are interspersed between the sense wires, forming a hexagonal structure. To resolve left-right ambiguity, each two adjacent layers are offset by half a cell. During the D_s data taking period, the CDC was never fully calibrated for position measurements. As a
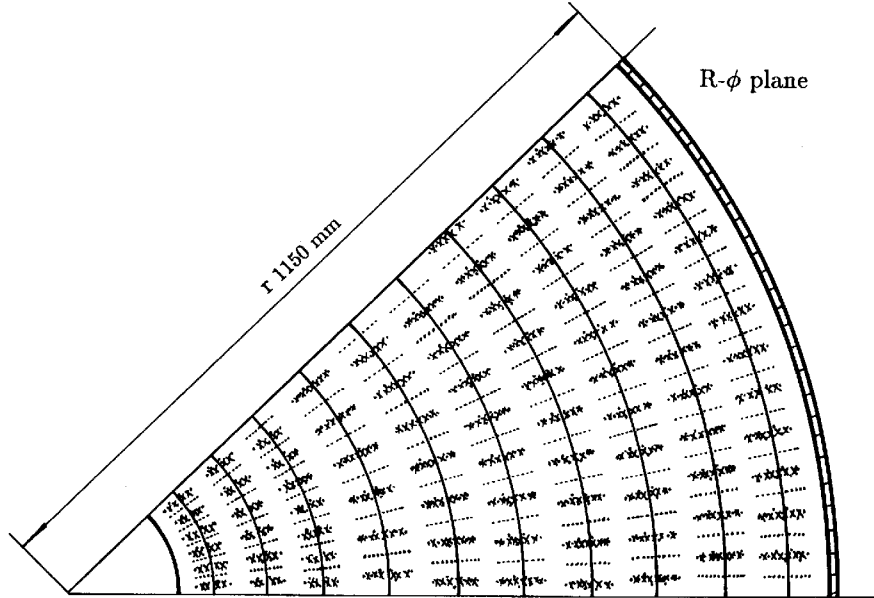
Figure 2.3: Cross-sectional view of the Main Drift Chamber

result, it was used solely for triggering purposes.

2.4 The BES Main Drift Chamber (MDC)

Since the CDC has been used only for triggering, all the information used in charged particle tracking comes from the main drift chamber (MDC). A 45° cross-section of the ρ-ϕ plane of the MDC can be seen in Fig. 2.3. There are overall 10 layers of cells, 5 axial layers (layers 2, 4, 6, 8, 10) and 5 stereo layers (layers 1, 3, 5, 7, 9), with the tilt angle of the stereo wires varying between 2 and 5 degrees. The axial layers provide information only for the ρ-ϕ coordinates of the track, whereas the stereo layers provide information for ρ,ϕ and z. Of the 10 layers, the four innermost ones are used for triggering. The number of cells per layer varies from 48 (in the innermost two layers) to 108 (in the outermost layer), totalling 702 cells. Each cell has 4 sense wires, bringing the total number of sense wires in the MDC to 2808.

Within each cell, the sense wires are 1cm apart, and they are offset alternately 350μ from the mid-plane of the cell, to resolve the left - right ambiguity of the tracks. The signal from the sense wires is used to measure both the electron drift time (the track position) and the drift charge (dE/dx). The overall performance of the system, in this respect, will be discussed in Chapter 3. The MDC runs on a continuous flow of an $Ar(89\%)$, $CO_2(10\%)$ and $CH_4(1\%)$ gas mixture. The inner diameter is 31.0 cm, the outer diameter 230.0 cm, and the overall length is 220.0 cm. The inner pipe is made of 2mm thick carbon fiber (equivalent to .009 radiation lengths) to minimize multiple Coulomb scattering. Both the outer cylinder and the end-plates are made of aluminum. Their thickness is 1cm and 4cm, respectively.

2.5   The BES Time of Flight System (ToF)

The Barrel ToF system consists of 48 NE110 scintillation counters arranged cylindrically between the Main Drift Chamber and the Barrel Shower Counter. Each counter measures 284 cm in length, 15 cm in width and 5 cm in thickness, and features a trapezoidal cross section to ensure more uniform ϕ - angle coverage. The total solid angle coverage for the barrel ToF is 76% of 4π.

On each side of a counter, light produced in the scintillator passes through an optical fiber, and gets collected with a XP2020 photomultiplier. To keep stray light from interfering with ToF measurements, both the scintillator and the optical fiber are packed with black paper and covered with aluminum. A magnetic screening structure also protects the photomultiplier from the leaking radial magnetic flux of the coil. Before installation, studies with cosmic rays, radioactive sources and laser light showed the inherent counter resolution and the counter attenuation length to be 200 ps and 236 cm, respectively. During our run, however, both these quantities had deteriorated significantly.

The endcap Time of Flight system has not been calibrated, and was not used during the Ds data-taking period.

Figure 2.4: Schematic view of the Barrel Shower Counter
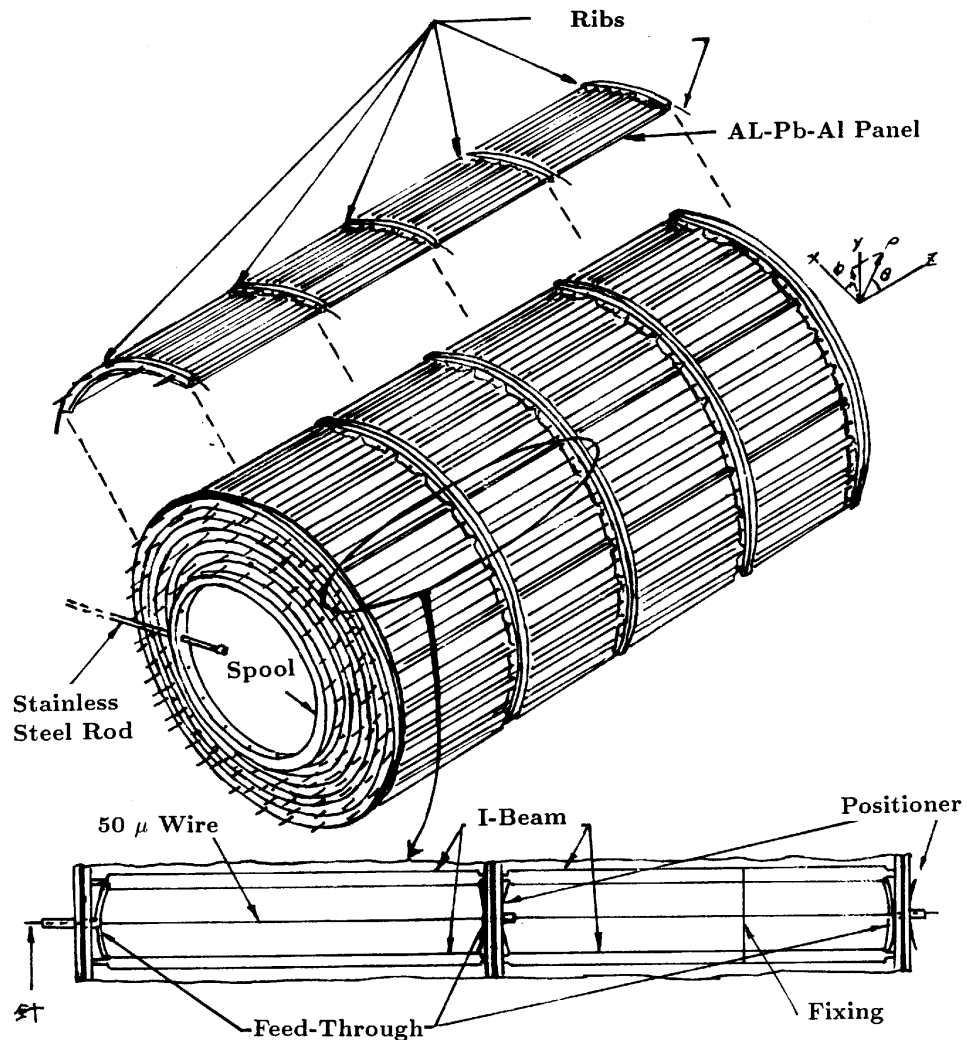
2.6 The BES Electromagnetic Calorimeter

The electromagnetic calorimeter consists of the Barrel Shower Counter (BSC) and the endcap shower counter (ESC). The general layout of the BSC can be seen in Fig 2.4. The BSC makes use of the gas discharge sampling method. It consists of 24 absorbing layers interspersed with 24 sampling layers. Each absorbing layer is made

up of ten similar sections of Al-Pb-Al sandwich with a total thickness of 3.6 mm (or 0.5 radiation lengths at the BES energies). Each sampling layer is separated into 560 cells by 1.3 cm high aluminum rods, positioned along the axis of the electron beam. The cells are filled with a $67\%CO_2 - 33\%Ar$ gas mixture, bubbled through with 0° C n-pentane, and operate in a self-quenching streamer mode. The z-position of the shower is determined by charge division between the two ends of the cell, whereas the ρ-ϕ position is simply determined by which cell is hit. During test runs, BES has measurd a z-resolution of 25mm, and a ϕ resolution of 4 mrad (limited by the cells' angular width). Energy resolution was $25\%/\sqrt{E}$, where E denotes the energy, expressed in GeV. The endcap shower counter was not calibrated during the D_s run. It was used in conjunction with the MDC to veto events with photons, if such a veto was desired.

2.7   The BES Muon Identifier

The BES muon identifier consists of 189 proportional muon counting tubes, interspersed with three layers of absorbing iron shields. It is schematicly shown in Fig. 2.5. The entire muon structure resides outside the soleinoidal coil, and the iron shield is also used as a flux return for the magnetic field.

Each counting tube has 8 single-wire cells, arranged in two offset layers to solve the left-right ambiguity problem. The z-position of the muon hits is determind by charge division between the two ends of the muon counter. The ϕ position is determined from the drift time, after calibration. The resolution thus attained has been 5cm in the z-direction, 3 cm in the ϕ direction.

2.8   The BES Luminosity Monitor – Measurement of Luminosity

The BES luminosity is measured by detecting small angle Bhabha events $e^+e^- \rightarrow e^+e^-$, and, from the measured rate, infer the luminosity of BES.
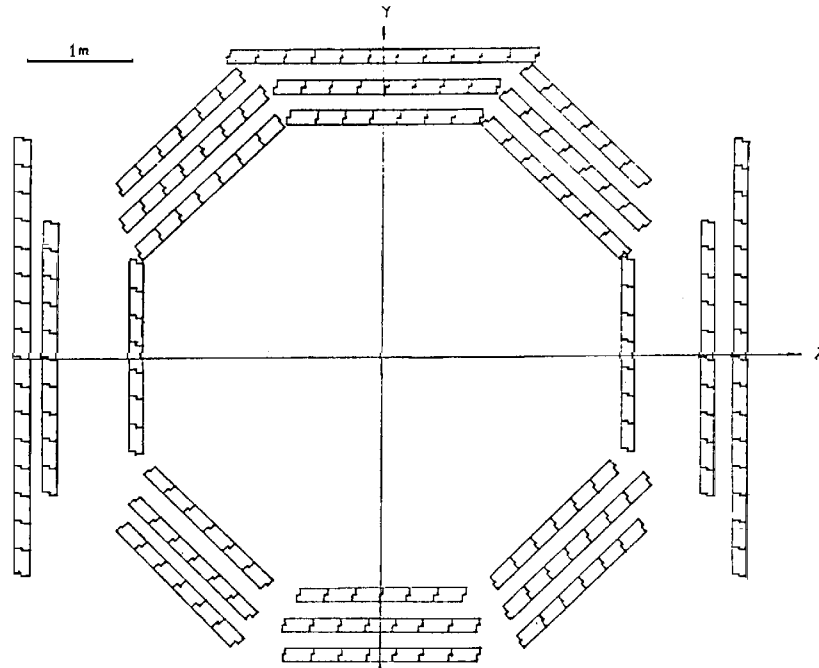
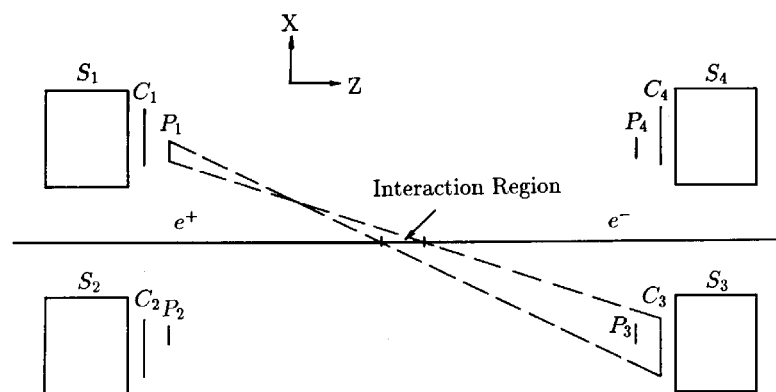Figure 2.5: Schematic view of the Muon Identification system

Figure 2.6: Schematic view of the Luminosity Monitor system

The geometry of the luminosity monitor can be seen in Fig. 2.6. P1...P4 and C1...C4 are plastic scintillator counters (designated "defining" and "complementary") that record a hit from a charged track. S1...S4 are lead-scintillator shower counters, which provide a measurement of the energy with 13% resolution. To account for a z-spread of the intercaction region of 5-6 cm, the dimensions of the P- and C-counters are such that if an electron (positron) from a bhabha event hits a primary (P) counter, the corresponding positron (electron) will intersect the diagonally opposite complementary (C) counter, no matter where in the interaction region the collision actually took place.

Three kinds of triggers were developed, to help increase the acceptance while reducing background:

a) **Normal Event Trigger:** P and S counters firing in one position, while the C and S counters fire in the diagonally opposite position. Essentially, this trigger requres the e^+e^- pair to geometrically intersect the C and P counters, while requiring corroboration from their respective shower counters.

b) **Delay Coincidence Trigger:** same as a), but with a time difference of one BEPC orbital period (802ns) between the hits in the P-counter position and the diagonally opposed C-counter position. This trigger was used to estimate the background from electron and positron bunches exciting the "correct" combination of counters independently, when passing from the luminosity monitor region.

c) **Random Sample Trigger:** all counters' information was recorded after 10^6 crossings, to account for all other sources of background.

To convert from the hit rate to the actual luminosity we used the Berends and Kleiss Monte-Carlo, taking into account radiative corrections and multiple scattering. However, due to the $(1/sin\theta)^4$ dependence of the Bhabha cross-section at small angles, the luminosity monitor is extremely sensitive to mechanical errors in the positioning of the primary counters. Therefore, during our run, the luminosity monitor information was only an estimate of the BES luminosity. The integrated luminosity figures quoted throughout this thesis were obtained from large-angle Bhabhas in four overlapping regions of of the BES detector.

To contribute to the large-angle Bhabha luminosity measurement, Bhabha candidates had to satisfy the following criteria:

- $N_{CHARGED} = 2$; total charge $= 0$; no isolated photons.

- $\cos\theta_{12} > 0.9$, where θ_{12} is the angle between the two tracks.

- $E_{shower} > 0.4(\frac{\sqrt{s}}{2})$ for each track

- $|P| > 0.5(\frac{\sqrt{s}}{2})$ for each track

- Vertex and Time Coincidence criteria

The total integrated luminosiy for the data set analysed in this thesis was estimated to be $22.9 \pm 0.7 pb^{-1}$. The main source of error is the uncertainty in the simulation of mechanical irregularities in the shower counter $(0.4\ pb^{-1})$. The error also gets sizeable contributions from the uncertainty in the higher-order QED calculation of the Bhabha cross-section $(0.25\ pb^{-1})$ and the anomalies in the azimuthal distribution caused by dead channels in the various detector systems $(0.35\ pb^{-1})$. Other contributions come from Monte Carlo statistics and trigger efficiency.

Chapter 3

Track Reconstruction and Particle Identification

3.1 Drift Chamber Single Track Finding and Reconstruction

The BES track finding and reconstruction code is largely based on the Drift Chamber code of Mark III, that was developped at SLAC between 1980 and 1989. The BES detector, however, has four sense wires per cell (compared to three in Mark III), so most of the code was modified accordingly.

The track search starts from the middle of the chamber, at layer 6, and initially employs only the axial layers. The code looks for a cell in which at least 3 out of the 4 sense wires are hit, and then reads the times for each wire's hit. Next, these times are turned to drift distances. Since at this stage only a crude estimate for the drift distance is desired, we assume a constant velocity v and neglect the Lorentz angle and the effect of the magnetic field. The distance then is found by:

$$D = v(T_{raw} - T_0 - \frac{A}{\sqrt{Q}})$$

A is a constant term, and the time-walk correction $1/\sqrt{Q}$ is introduced to compensate for the effects of the leading-edge pulse shape on the electronics trigger.
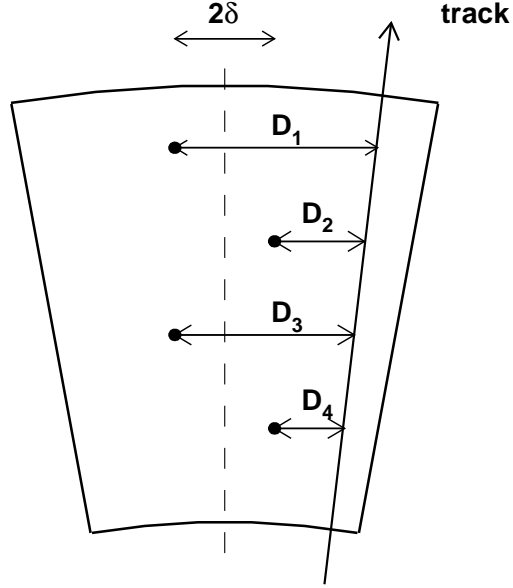
Figure 3.1: Local left-right ambiguity resolution in the cell. The heavy dots correspond to the positions of the sense wires

The next step is to solve the left-right ambiguity for the track (see Fig 3.1). If we ignore the inherent wire resolution, assume a locally straight track, and a drift path perpendicular to the axis of the cell, then for each triad of consecutive, staggered wires i,j,k the residual

$$\epsilon_{ijk} = (D_i \pm \delta) + (D_k \pm \delta) - 2(D_j \mp \delta)$$

should be zero if, for each term, we assign the positive (negative) sign every time the track lies to the same (opposite) side as the wire's stagger displacement. In reality, ϵ_{ijk} has a finite spread due to a wire position resolution of approximately 250 microns:

$$\sigma(\epsilon) = \sqrt{6}\sigma_{wire}$$

or about 0.7 mm. Assigning the wrong sign combination, though, will generally produce a residual much larger than $\sigma(\epsilon)$. If, for example, we moved the track of Fig. 3.1) to the left side of the cell, we would have

$$\epsilon_{left} - \epsilon_{right} = 8\delta \approx 3mm$$

which would indicate that ϵ_{left} clearly corresponds to the wrong choice.

To take advantage of all four possible hits in the BES cells, the code actually calculates the quantity

$$\chi^2 = |\epsilon_{123}| + |\epsilon_{234}|$$

for all 16 sign combinations. The sign combination that corresponds to the lowest χ^2 determines the left-right position of the track. If the assignment is ambiguous (i.e. if the two lowest residuals lie too close together), each wire's information is successively ignored, and the procedure is repeated until an unambiguous left-right assignment can be made. If this is not possible, the code proceeds to the next layer along the search. Having resolved the left-right ambiguity, we have a first, crude estimate of a position and a tangent for the circle of the track. With this information, the code extrapolates the arc, and calculates the intersections of the circle with the other axial layers. Then it looks for hits in the cells located on these intersection points, or in their nearest neighbors. If more than 12 such hits are established, the code proceeds to do the first circle fit, using Ascoli's method [28]. First it loops through all relevant axial layers, getting one extra layer's information each time, and re-fitting iteratively. Then it loops through all stereo layers, and fits to a straight line for the z-position of the track. If the line extrapolates to a reasonable distance around the interaction region, then the code repeats the circle fit, this time with information from both stereo and axial layers. If the χ^2 of the fit is too large, up to 5 points get dropped, and the fit is repeated.

If the circle and the z-fit point to a good track, then the track is re-fitted, using a piecewise helical path that accounts for the slight non-uniformity of the magnetic field. The drift distance is parametrized along three separate regions, to take into account the drift field map and the Lorentz angle: The drift electrons originally accelerate in the "far-field" region, then drift at a contant velocity in the "constant

field" region, and finally travel radially inward to reach the wire, in the "near-field" region. In other words, we have:

$$D_n = (t - t_n)v_n$$
$$D_c = (t - t_c)v_c \cos\theta$$
$$D_f = (t - t_f)^2 v_f$$
$$D.C.A = D_n + D_c + D_f$$

Here t_n, t_c, t_f are the times indicating the boundaries of the "near", "constant" and "far" - field regions; v_n, v_c and v_f are the respective velocities (actually, v_f has units of acceleration). D.C.A is the Distance of Closest Approach.

The helix is described in terms of six parameters:

- the inverse of the tranverse momentum $(1/P_T)$

- the cosine of the dip angle $(k \equiv \cos\theta)$

- the azimuthal angle ϕ at the point of closest approach, and

- the x, y and z coordinates of the point of closest approach.

To get the best fit values for those, the code starts from the parameters of the original circle- and z- fits, and iterates, using a linear matrix approximation. In each iteration, it perturbs the input values of the parameters, to get the matrix M:

$$M_{ij} = \left[\sum_l \frac{\frac{\partial f_l}{\partial \alpha_i} \frac{\partial f_l}{\partial \alpha_j}}{\sigma_l^2} \right]$$

where the summation index l runs over all the hit points, $\alpha_{i,j}$ are the helix parameters, and f_l is the distance betweem the actual hit coordinates (as given by the MDC) and the corresponding point on the analytic helix. The code then inverts M_{ij}, to get a new set of parameters. This procedure is repeated, until the χ^2 of the fit stops improving. If the total final χ^2 of the fit is less than 250, then the track is considered to have passed the helix fit, and the track parameters and error matrix entries are filled. If the track fails the helix fit (but passes the seperate circle and z-fits) then the track parameters are filled, but not the error matrix. About 4% of all BES tracks fall under the latter category.

Following the procedure described above, the BES main drift chamber has a single track geometric acceptance of 85% of 4π, with reconstruction efficiency $\geq 99\%$. The inherent z resolution is 0.9 cm, and the transverse momentum resolution for individual charged tracks scales as

$$dP/P = 2.1\%\sqrt{1 + P^2}$$

if P is expressed in GeV/c.

3.2 Particle Identification

The two main, overlapping systems of particle identification used in this analysis were the Time of Flight (ToF) counters, and the dE/dx information from the main drift chamber. What follows is a brief account of the performance of each system:

3.2.1 Time of Flight

The "raw" times that come out of the ToF electronics have to be corrected to account for the transit time of the photomultipliers, the length of the cables, the position of the hit on the ToF counter, and the charge-dependent "time walk" effect (see section 3.1). For a single end of the ToF counter, the calibrated time becomes:

$$T = T_{RAW} - T_0 - \frac{A_1 + A_2 Z}{\sqrt{Q}} - \frac{A_3 + A_4 Z}{Q} - A_5 Z - A_6 Z^2 - A_7 Z^3$$

Here T_{RAW} is the time from the counter's ADC (converted to nanosecond units), Q is the integrated pulse size, and Z is the intersection of the track's path with the ToF counter, as projected from the MDC information. As in the MDC calibration, the "time walk" correction accounts for the effect of the pulse shape on the trigger electronics. The linear Z coefficient A_5 roughly corresponds to $(1/v)$, where v is the goup velocity of light in the scintillator (for most counters, $v \sim 0.6c$). Finally, the higher order terms account for the pulse shape distortion from multiple reflections and multiple photon emissions.

For most well-defined tracks, we get a signal from both ends of the ToF counter.

Then the time is calculated as a weighted sum of the individual ends' measurements:

$$T = (w_1 T_1 + w_2 T_2)/(w_1 + w_2)$$

The constants $(A_1, \ldots, A_7)$, as well as the weights W_1, W_2, are determined by the off-line ToF calibration. This is performed with Bhabha events, selected independently of the ToF system. Since the electron's path length L is measured in the MDC with very good accuracy, and the electron's velocity is essentially c , the calibration tries to minimize, for each end, the residual:

$$\chi = |T(A_1 \ldots A_7, T_0) - L/c|.$$

We first determine the "primary" coefficients (A_1, A_2, A_5) and then determine the higher order corrections. The fit is repeated iteratively until it converges. Next, we perform a second, separate fit for the weighting factors w_1, w_2. We assume a functional form for the weights:

$$w = b_1 + b_2 Z + b_3 Z^2$$

and search for values (b_1, b_2, b_3) that minimize the overall residual:

$$\frac{w_1 T_1 + w_2 T_2}{w_1 + w_2} - L/c$$

To produce meaningful results, the calibration required about 150 tracks per counter, (equivalent to ~3500 Bhabha pairs), and generated a new set of constants for every two to three day's worth of data.

In Fig. 3.2 we can see the quantity $T - T_{expected}$ plotted against the particle momentum, for the four particle ID hypotheses for each track: electron, pion, kaon and proton. We observe that, even though the graphs display the correct general characteristics, and the electron band of Fig. 3.2 is, by construction, centered, arrival times are systematicly offset for pions, kaons and protons. For a given momentum, the offset is more pronounced for the more massive particle.

This offset seems to be correlated with the particle's β (or, equivalently, the average charge deposited for a given z-coordinate and angle of impact): the calibration employed Bhabha electrons, which are minimum ionizing particles. Low momentum

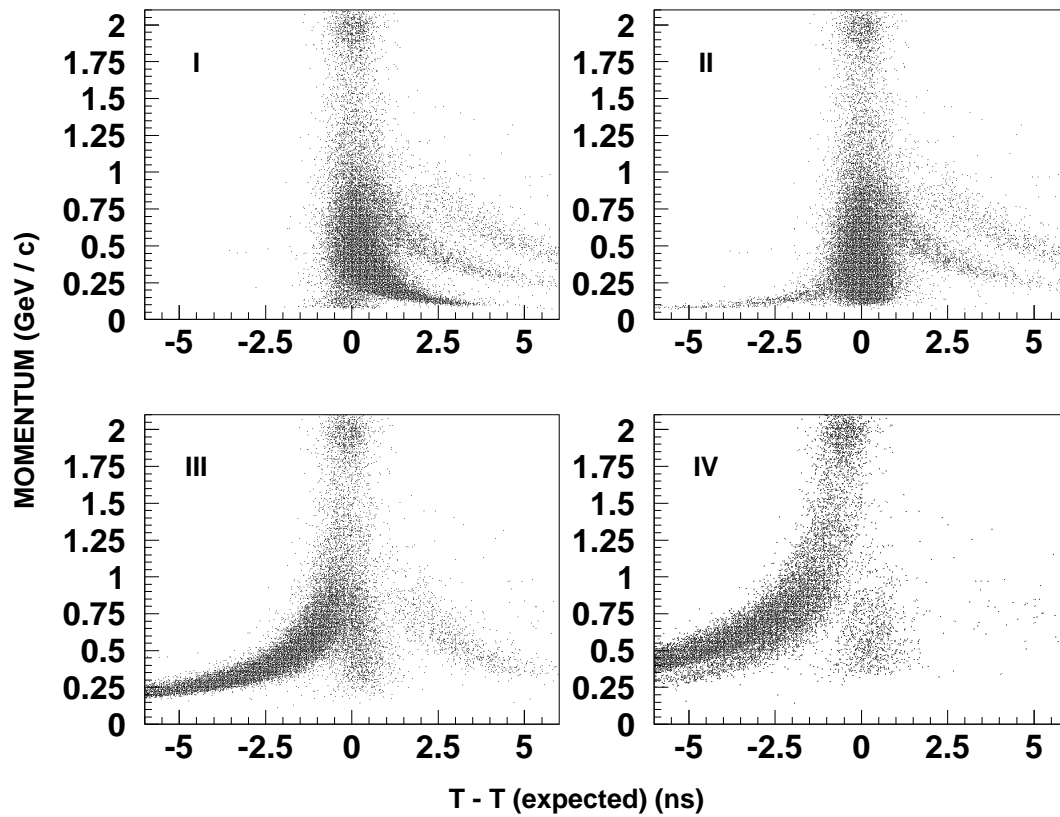Figure 3.2: The quantity $T - T_{expected}$ (in nanoseconds) vs. momentum (in GeV) for electrons (I), pions (II), kaons (III) and protons (IV). Note the offset for low momentum kaons and protons.
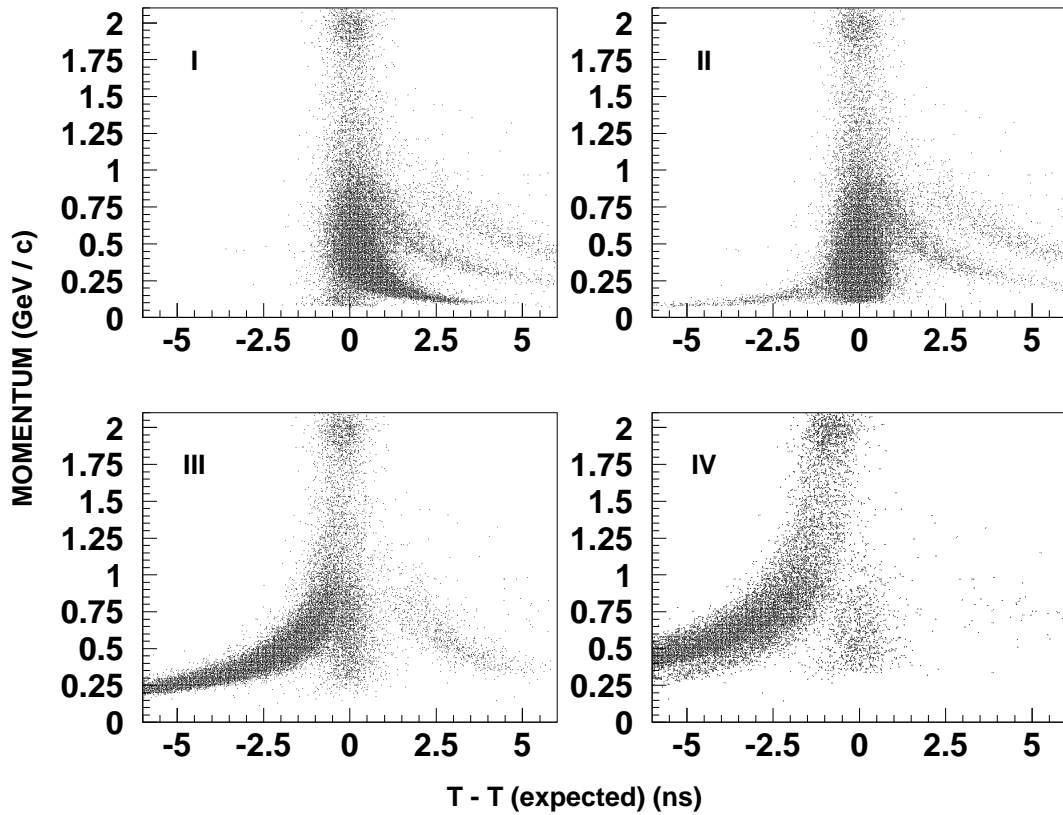
Figure 3.3: $T - T_{expected}$ vs. momentum for electrons (I), pions (II), kaons (III) and protons (IV), after the T_{COR} corrections. The electrons were not corrected, but the electron plot is shown here for completeness

hadrons, on the other hand, tend to have much higher average pulse heights. Apparently, the ToF correction formula that was derived for low pulse heights does not extrapolate correctly to the high pulse height region. At BES we attempted to correct for the offset analytically, by adding more parameters to the ToF correction formula, doing a piecewise calibration for different portions of the counter, or supplementing the calibration sample with dimuons to counteract for the effects of stray electron showers in the endplate distorting the photomultiplier readings. None of these methods produced any noticeable improvements, so we ended up cancelling the offset by inputing a separate ToF correction function in the BES analysis:

$$T \rightarrow T - T_{COR}$$

T_{COR} was a data-driven correction that depended on the particle's momentum, position and angle of impact, and particle ID hypothesis. The new, corrected times are shown in Fig. 3.3.

T_{COR} centered the Δ_{TOF} distributions, but it still left the hadron ToF resolution somewhat higher that that for Bhabhas. As the ToF counters sustained more and more radiation exposure, the attenuation length shortened, and resolution progressively deteriorated. The average ToF resolution for the whole data sample was 380 picoseconds for Bhabhas and 445 picoseconds for hadrons.

3.2.2 dE/dx

The dE/dx system shares hardware with the Main Drift Chamber readout system. The pulse information is stored in a Sample Hold Analog Module (SHAM), which integrates the signal over the duration of the pulse and outputs a raw dE/dx charge for each hit. This charge is then scaled for the variation in dE/dx collection length for the different angles of incidence for the track, and corrected for wire gain, drift distance, and the space saturation of the gas. The individual pulse heights (up to 40 for a given track) generally fall along a Landau distribution . The code, however, does not fit the hits to an analytical Landau function. Instead, it uses the "truncated mean" approach: the highest 30% of the hits are ignored, and the code simply averages
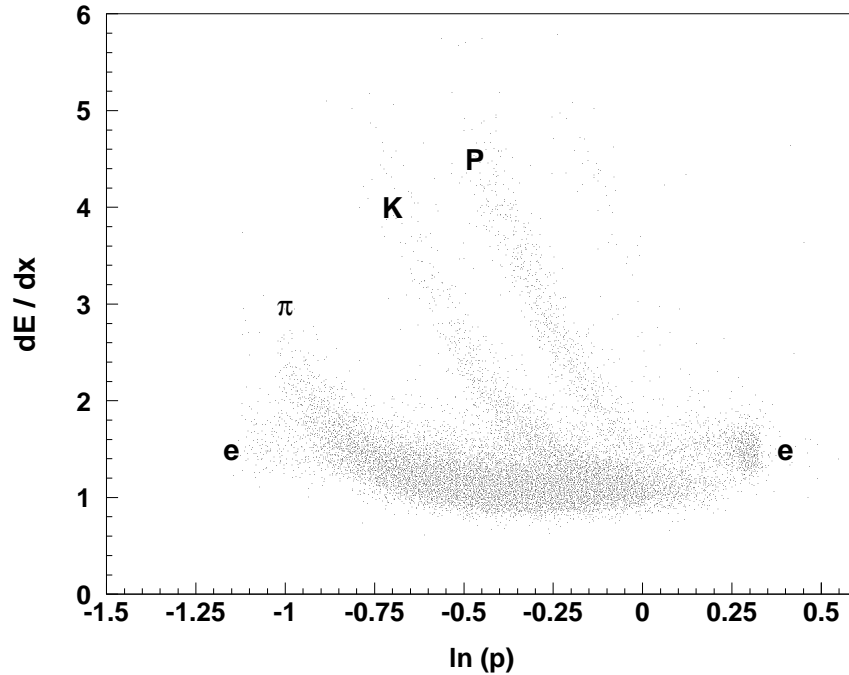
Figure 3.4: dE/dx for charged tracks at BES. The x-axis shows the logarithm of the momentum. The dE/dx units roughly correspond to a keV/cm

the rest. This is done to save CPU time and to avoid the effect of one outlier hit skewing the fits, thereby leading to a wrong dE/dx assignment for the track.

The dE/dx calibration constants are determined by iterative fitting. Electrons, pions, kaons and protons, selected independently of the dE/dx system, are used to probe different β regions of the dE/dx curve. For each sample, we calibrated each individual layer separately, so as to minimize both the deviation between measured and predicted dE/dx value and the spread of the measurements around the desired mean. For the purposes of this analysis, the dE/dx signal was also corrected globally, taking into account the calculations of VaVra *et al.* [29] as applied to the BES drift chamber and gas mixture. The dE/dx plot for the charged particles at BES is shown in Fig. 3.4.
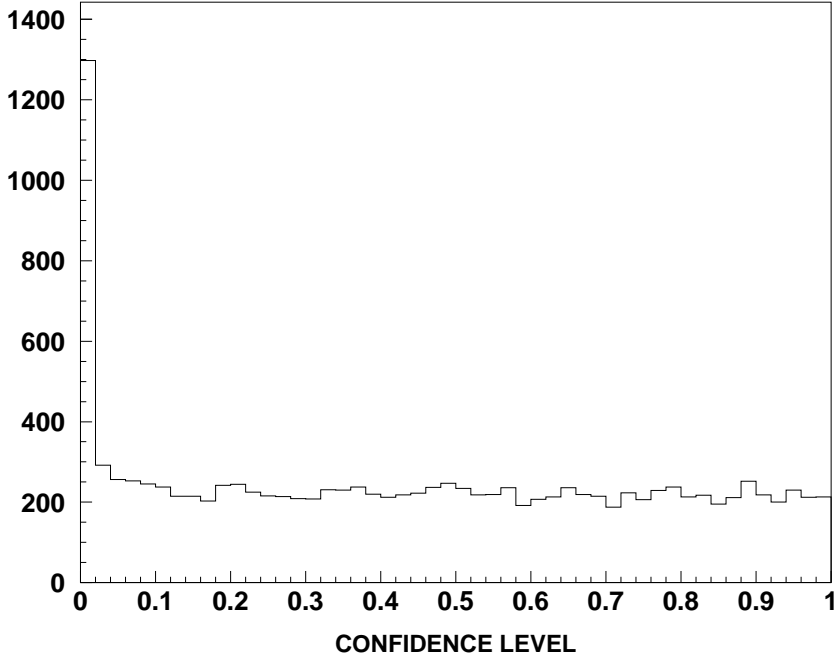
Figure 3.5: Confidence Level distribution for pions from kinematically selected $J/\psi \rightarrow \omega\pi\pi, \omega \rightarrow \pi\pi\pi_0$ events

For hadrons, the overall normalized resolution was

$$\frac{\sigma_{dE/dx}}{dE/dx} \simeq 11\%$$

3.2.3 π/K Separation

For the purposes of this analysis, particle identification consisted of separating pions and Kaons using the ToF and dE/dx. To take advantage of the two independent, redundant particle ID systems, we built a normalized likelihood ($\mathcal{L}$) and a confidence level (CL) using both ToF and dE/dx information:

$$\mathcal{L}_{K/\pi} = \frac{e^{(-1/2)[(\Delta_{TOF}^{K/\pi})^2+(\Delta_{dE/dx}^{K/\pi})^2]}}{e^{(-1/2)[(\Delta_{TOF}^{K})^2+(\Delta_{dE/dx}^{K})^2]} + e^{(-1/2)[(\Delta_{TOF}^{\pi})^2+(\Delta_{dE/dx}^{\pi})^2]}}$$

where

$$\Delta_{TOF}^{K/\pi} = \frac{TOF_{measured} - TOF_{expected}^{K/\pi}}{\sigma_{TOF}}$$

$$\Delta_{dE/dx}^{K/\pi} = \frac{dE/dx_{measured} - dE/dx_{expected}^{K/\pi}}{\sigma_{dE/dx}}$$

and the confidence level is calculated by:

$$CL = \int_{\chi^2}^{\infty} f(Z;n)dZ, \qquad f(Z;n) = \frac{Z^{n/2-1}}{2^{n/2}\Gamma(n/2)}e^{-Z/2}$$

Here n denotes the number of systems providing information, and the residual χ^2 is defined as:

$$\chi^2 \equiv (\Delta_{TOF})^2 + (\Delta_{dE/dx})^2$$

If the ToF information was absent or of poor quality, we only used the dE/dx system; n became equal to 1 and the χ^2 definition was modified accordingly. The confidence level distribution for pions kinematically selectrd through the process $J/\psi \to \omega\pi\pi, \omega \to \pi\pi\pi^0$ can be seen in Fig. 3.5. For most applications, we required a confidence level greater that 1% for both Kaons and Pions. Also, we required the normalized Kaon likelihood to be greater that 0.5, in order to positively identify a Kaon. For well reconstructed tracks, this method allowed for K/π separation up to a momentum of approximately 540 MeV.

Chapter 4

Analysis: D_s single tag decays

4.1 Introduction – General Remarks

This chapter will describe the search for the inclusive D_s production. The D_s is tagged via four hadronic decay modes, namely:

- $D_s \to \phi\pi$; $\phi \to K^+K^-$

- $D_s \to \overline{K^{*0}}(892)K$; $\overline{K^{*0}}(892) \to K^-\pi^+$

- $D_s \to \overline{K^0}K$; $\overline{K^0_s} \to \pi^+\pi^-$

- $D_s \to \overline{K^{*0}}(892)K^{*0}$; $\overline{K^{*0}}(892) \to K^-\pi^+$; $K^{*0}(892) \to K^0\pi^+$; $K^0_s \to \pi^+\pi^-$

Despite the differences in the modes' configurations, the main characteristics of the tagging procedure for each mode were rather similar:

First, we would loop over all charged tracks in an event, and select a set of tracks with particle ID assignments consistent with the decay products of the particular mode. Following the method of section (3.2.4), to accept a track as a Kaon we required a confidence level consistency higher than 1% and a likelihood preponderance of the Kaon hypothesis:

$$CL_K \geq 0.01$$

$$\frac{\mathcal{L}_K}{\mathcal{L}_K + \mathcal{L}_\pi} \geq 0.5$$

For a pion, on the other hand, we simply required a confidence level consistency:

$$CL_\pi \geq 0.01.$$

Next, we imposed the necessary intermediate mass constraints, to reduce backgrounds and non-resonant contributions, and calculated the invariant mass for the combination:

$$M_{INV} = \sqrt{(\sum_i E_i)^2 - |\sum_i \vec{P_i}|^2}$$

where the index i ran over all the tracks in the combination, and the energy E_i was calculated according to the (assumed) particle ID assignment for the ith track. For the four modes mentioned above, Monte Carlo studies showed the resolution of M_{INV} to vary from 25 to 35 MeV. Therefore all combinations with M_{INV} greater than 2.15 GeV or less than 1.80 GeV (or about 5σ away from the nominal D_s mass) were subsequently ignored.

Finally, the combinations that remained were subjected to a "1-Constraint (1-C) Kinematic Fit", using the TELESIS software package from Mark III. The principle behind the Kinematic Fitting procedure can be described as follows: At $\sqrt{s} = 4.03$ GeV, the D_s mesons are produced exclusively in particle-antiparticle pairs, with each D_s carrying precisely half the beam energy. Therefore, if all tracks in the decay are detected and particle ID is assigned correctly, the total energy of the D_s decay products should equal $\sqrt{s}/2$, or 2.015 GeV. In practice, however, this doesn't happen, because of the finite momentum resolution of the detector. The kinematic fitter, when given such a set of tracks, modifies, for each track, the initial set of relevant track parametes (here $(1/P_{XY})_{initial}$ $(cos\theta)_{initial}$ and $\phi_{initial}$) into the values $(1/P_{XY})_{final}$, $(cos\theta)_{final}$, and ϕ_{final} so as to minimize the quantity

$$\chi^2 = (X_{final} - X_{initial})^t M^{-1} (X_{final} - X_{initial})$$

subject to the constraint $E_{final} = 2.015$ GeV. Here X is the vector $(1/P_{XY}, cos\theta, \phi)$, and M is the covariance matrix in these same three variables. Then the "1-C fitted Mass" is defined as:

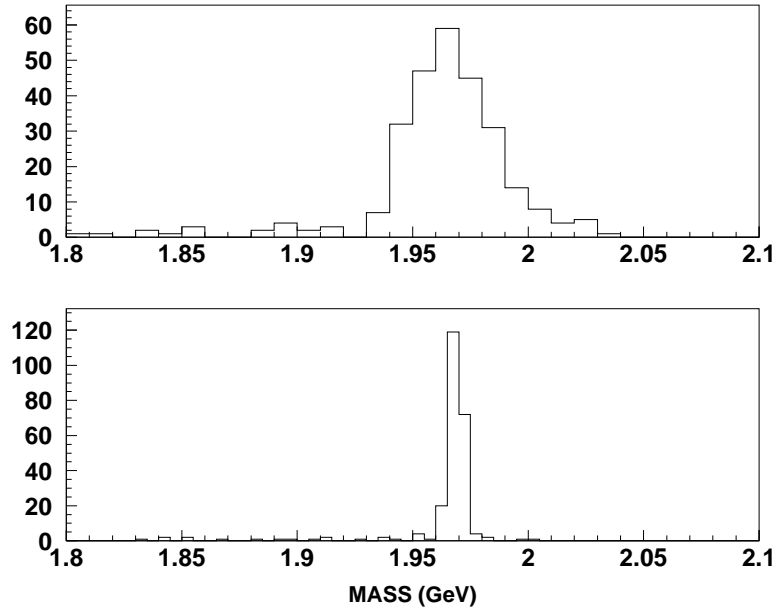$$M_{FIT} = \sqrt{(\frac{\sqrt{s}}{2})^2 - |\sum_i \vec{P}_i^{final}|^2}$$

Figure 4.1: Invariant (top) and fitted (bottom) mass from $D_s \to \phi\pi$ Monte Carlo

where i, again, sums over all tracks in the combination. The fit is accepted if the minimum χ^2 corresponds to a user-specified minimum confidence level. Monte Carlo studies have shown the 1-C fitted mass to have a resolution of approximately 4–6 MeV, a very significant improvement over the resolution of the invariant mass (see Fig 4.1).

In sections 4.3 through 4.6, I will describe in more detail the application of this general method to the four modes mentioned in the beginning of this section. I will also discuss some additional measures we employed to reduce backgrounds, and present the numerical results of our single-tag D_s search. First, however, I will offer a brief account of our background considerations and Monte Carlo techniques.

4.2   Monte-Carlo Simulation; Background Studies

Monte Carlo simulation was our primary tool for determining efficiencies and studying the different backgrounds. The BES Monte Carlo was centered around the SOBER (Simulation Of BES Reconstruction) software package, which was inherited from Mark III. The detector response simulation would take into account the inherent systems' resolutions, layer efficiencies, energy loss in the detector material, and multiple Coulomb scattering. For each particle type and momentum, the dE/dx hits were produced along a Bethe-Bloch formula, and were randomly varied by a resolution σ, where $\sigma_{dE/dx}/(dE/dx) \sim 11\%$. The Time of Flight resolution was determined for each counter using real pion tracks, selected by dE/dx with strict criteria to avoid contamination. The simulation would also take into account the variations in an individual counter's resolution due to the track's geometry and the amount of charge deposited in the scintillator. As the characterisics of the detector changed over time, we created a separate structure (BES-REALIZATION) that allowed users to generate data simulating the detector's performance for a particular running period.

Individual genetators were used to simulate the following processes:

$e^+e^- \rightarrow D_s^+ D_s^-$

$e^+e^- \rightarrow D^* \overline{D}$

$e^+e^- \rightarrow D^* \overline{D^*}$

$e^+e^- \rightarrow D \overline{D}$

$e^+e^- \rightarrow q\bar{q}(g)$ for u, d, and s quarks.

We based our D and D^* meson production cross-sections on preliminary BES results by Chen ShaoMin [30]:

$$
\begin{aligned}
\sigma_{D^{*0}D^0} &\approx \sigma_{D^{*\pm}D^{\mp}} &\approx 3.5\,\text{nb} \\
\sigma_{D^{*0}D^{*0}} &\approx \sigma_{D^{*+}D^{*-}} &\approx 1.0\,\text{nb} \\
\sigma_{D^0D^0} &\approx \sigma_{D^+D^-} &\approx 0.2\,\text{nb}
\end{aligned}
$$

For the non-charm continuum simulation we employed the JETSET 6.3 generator, based on the LUND fragmentation model [31]. At 4.03 GeV, LUND estimates the $q\bar{q}(g)$ cross-section to be 11.8 nb. All relevant background figures normalize these cross-sections to the total integrated BES luminosity of 22.9 pb.

4.3 $D_s \to \phi\pi$

We started our D_s search with the $D_s \to \phi\pi$ mode, since this decay is relatively abundant and background-free. $D_s \to \phi\pi$ was first observed by CLEO in 1983, and, by convention, has provided the normalization for the branching fractions of all other observed D_s decays.

Our first task was to tag a clear ϕ signal, through the decay $\phi \to K^+K^-$. We only considered events with 3 or more good quality charged tracks. The invariant mass of all positively identified kaon pairs is shown in Fig. 4.2. We observed a clear signal in the ϕ mass region, and obtained a ϕ mass of 1019±1 MeV, and a width of 4.5±.3 MeV. Both numbers are consistent with the Particle Data Group values [35].

Next we combined all kaon pairs with a pion, and calculated both the Invariant Mass (M_{INV}) and the 1-C fit mass (M_{FIT}) for the three tracks. We imposed a 5% confidence level cut in the 1-C fit. For all the combinations that survived the 1-C fit cut, and had M_{INV} in the window $1.80~GeV \leq M_{INV} \leq 2.1~GeV$, we see the scatterplot of M_{FIT} against the mass of the kaon pair in the bottom of fig. 4.2. We can observe the enhancement where $M_{KK} \sim 1.019$ GeV and $M_{KK\pi} \sim 1.97$ GeV, as is expected from the decay $D_s \to \phi\pi$; $\phi \to K^+K^-$. We also note that, outside the $\phi - \pi$ mass region of the plot, the entries are distributed more or less uniformly (there are no discernible ϕ and D_s bands along the $x-$ and $y-$ axes, respectively). This indicates that:

1. In the neighborhood of the ϕ resonance, there is no significant non-resonant $KK\pi$ contribution to the $D_s \to KK\pi$ decay, and

2. There is no significant ϕ production associated with the sources of background in the $D_s \to \phi\pi$ mode.

To reject the non-ϕ contributions, we then kept only the $KK\pi$ combinations in which the invariant mass of the kaon pair was within 15 MeV (or $\sim 3~\sigma$) of the nominal ϕ mass. Finally, to further reduce the background, we employed a cut in the helicity angle cosine of the $\phi\pi$ system: Since $J^P(D_s) = 0^-$, $J^P(\phi) = 1^-$ and $J^P(\pi) = 0^-$, the distribution of the decay $D_s \to \phi\pi$ in the variable $cos\theta_{HEL}$ (the helicity angle,
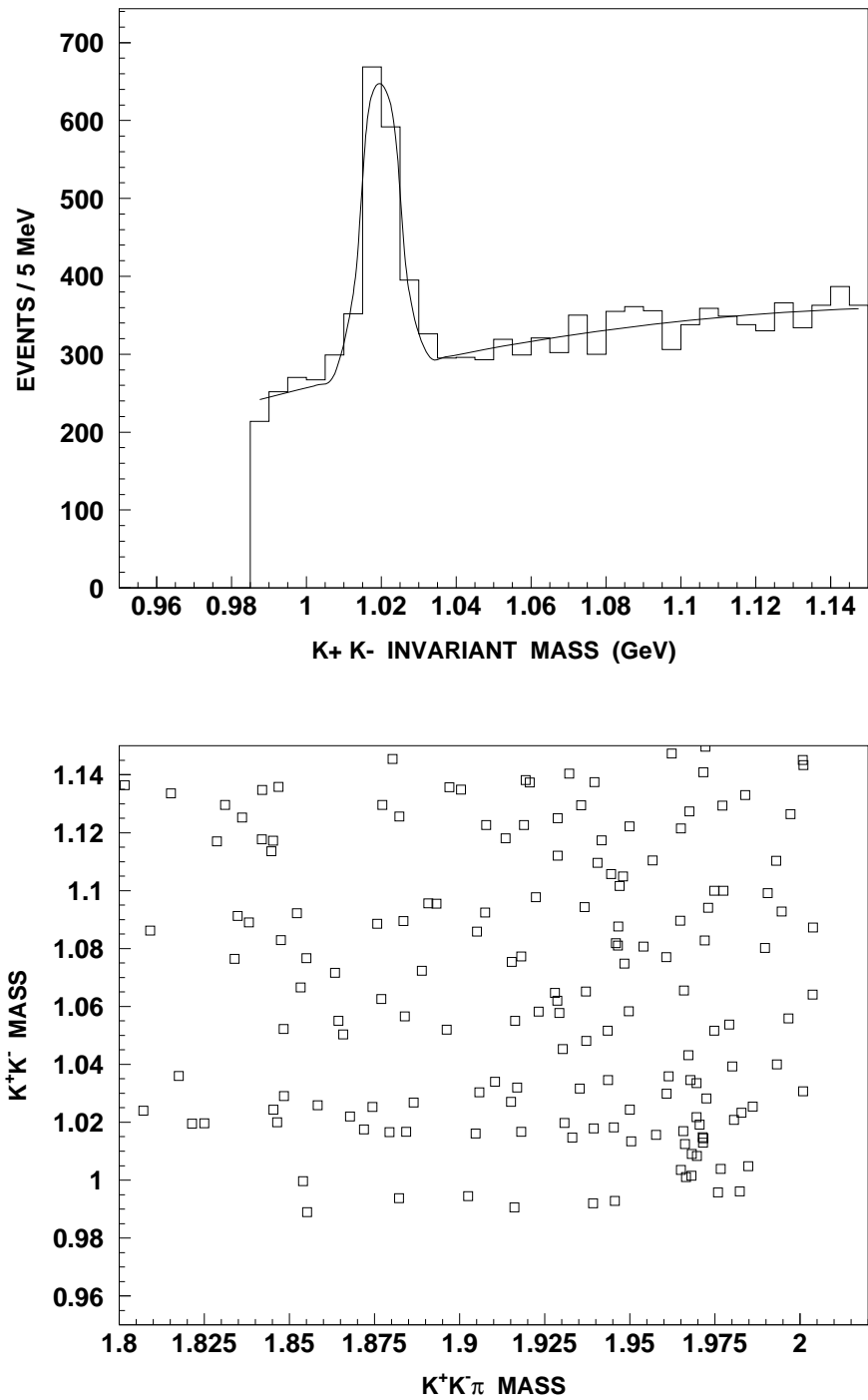
Figure 4.2: The K^+K^- invariant mass spectrum (top) and the scatterplot of m_{KK} against $m_{KK\pi}$ (bottom)
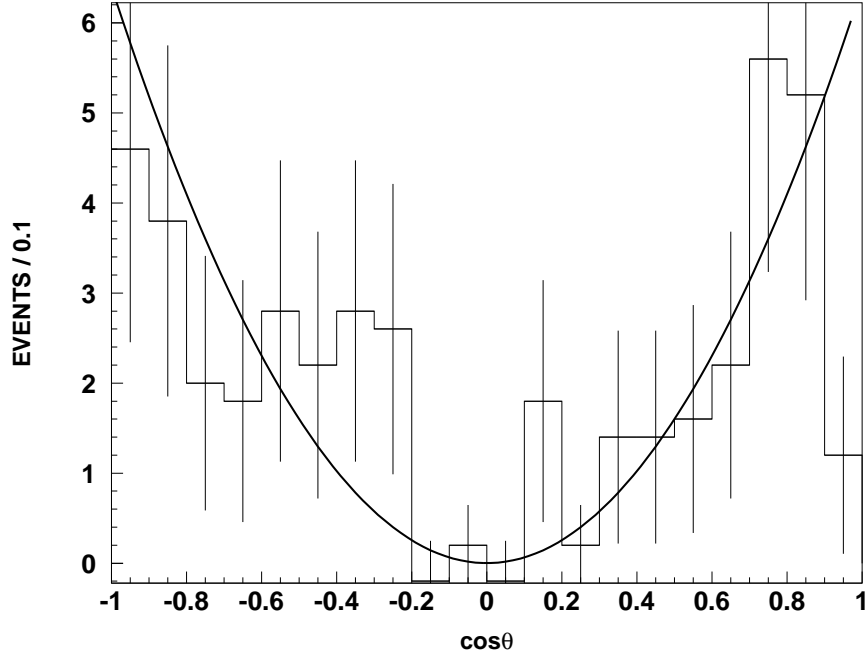
Figure 4.3: Cosine of the Helicity angle of the $\phi\pi$ system for the D_s signal region, after sideband subtraction. the solid curve corresponds to the theoretical prediction of a $cos^2\theta$ distribution

in the ϕ frame, between the momentum of either kaon and the momentum of the "incoming" D_s) should vary as $cos^2\theta_{HEL}$ (Fig. 4.3). We set the helicity cosine cut at $|cos\theta_{HEL}| \geq 0.25$; this cut reduces the background substantially, without affecting the signal in any appreciable way. The final mass plot, after all the above mentioned cuts, is shown in Fig. 4.4. An unbinned maximum likelihood fit estimates the number of entries under the peak $(N_{\phi\pi})$ at 43 ± 7 events; the D_s mass at 1968.2 ± 0.9 MeV, and the fit mass resolution at 4.3 ± 0.6 MeV. A Gaussian signal was assumed, over a polynomial background constrained by two phase space factors. The mass assignment is in good agreement with the Particla Data Group average of 1968.5 ± 0.7 MeV.

Knowing $N_{\phi\pi}$, we can calculate the product of the D_s pair production cross-section
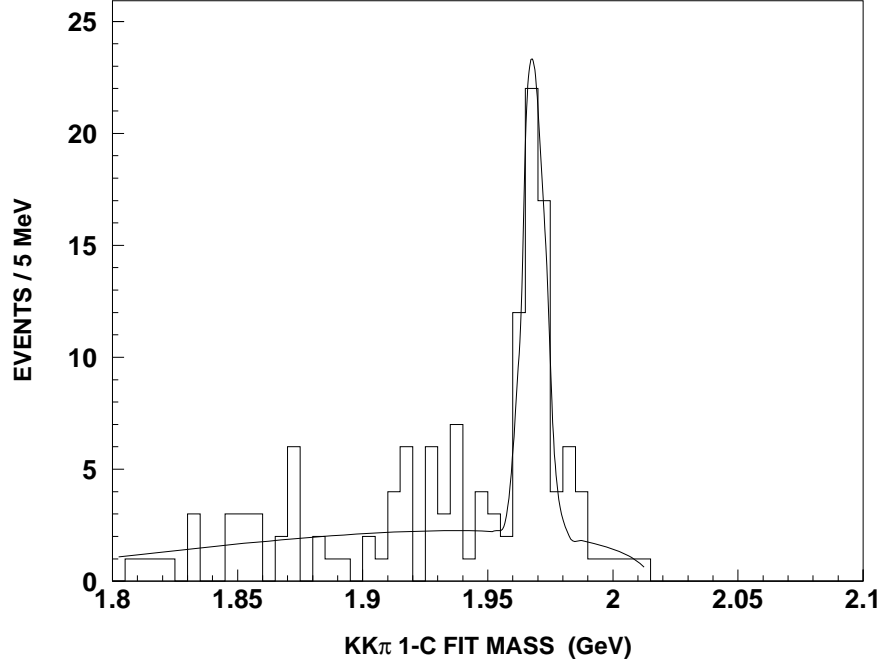
Figure 4.4: $KK\pi$ 1-C fitted mass spectrum. The shape of the background corresponds to a polynomial constrained by two phase space factors; the signal is assumed Gaussian

and the $D_s \rightarrow \phi\pi$ branching fraction. It is given by the formula

$$\left(\sigma_{e^+e^- \rightarrow D_s^+ D_s^-}\right) \cdot \left(Br_{D_s \rightarrow \phi\pi}\right) = \frac{N_{\phi\pi}}{2\epsilon_{\phi\pi} \int \mathcal{L}dt}$$

where $\epsilon_{\phi\pi}$ is the reconstruction efficiency for the $\phi\pi$ mode, and $\int \mathcal{L}dt$ is the total integrated luminosity of the analyzed data sample. The reconstruction efficiency, including the $\phi \rightarrow K^+ K^-$ branching fraction, is estimated by Monte Carlo simulation to be 8.4±0.3%. Given our values for luminosity and $N_{\phi\pi}$ of $22.9 \pm .7 \, \text{pb}^{-1}$ and 43 ± 7 events respectively, we get:

$$\left(\sigma_{e^+e^- \rightarrow D_s^+ D_s^-}\right) \cdot \left(Br_{D_s \rightarrow \phi\pi}\right) = 11.1 \pm 1.8 \pm 1.1 \, \text{pb}$$

where the first error is statistical and the second is systematic. The systematic error

includes contributions from the error in the luminosity measurement, as well as from variations in the selection criteria, the background parametrization, and the efficiency determination.

Taking into account the present world average for $Br_{D_s \to \phi\pi}$ of 3.5±0.4%, we find the $D_s^+ D_s^-$ production cross-section at 4.03 GeV to be:

$$\sigma_{e^+e^- \to D_s^+ D_s^-} = 317 \pm 52 \pm 47 \, \text{pb}.$$

This is significantly lower than the value of 750 pb predicted by the Eichten model. No convincing explanation has been offered for this discrepancy.

4.4 $D_s \to \overline{K^{*0}}(892)K; \ \overline{K^{*0}}(892) \to K^-\pi^+$

The $D_s \to \overline{K^{*0}}(892)K$ mode is similar to the $\phi\pi$ mode, in that they are both quasi-two-body decays, and have the same spin-parity configuration $(0^-) \to (1^-)(0^-)$. However, in the $\overline{K^{*0}}(892)K$ mode there are two additional cosiderations:

1. Due to the large width and contamination under the K^{*0} resonance, there is a lot of non-K_0^* related background in the final D_s mass plot, and

2. K^{*0} decays of the D-mesons (from the DD^* and D^*D^* background) reflect into narrow peaks close to the D_s mass region.

We started the search for the $\overline{K^{*0}}(892)K$ mode by calculating the invariant mass of all $K^\mp\pi^\pm$ combinations in events with more than 3 good-quality charged tracks, to identify a $K_0^* \to K^+\pi^-$ mass peak (Fig. 4.5). We imposed a confidence level cut for both kaons and pions, and a normalized likelihood cut for the kaons. Fitting the peak to a Breit-Wigner, we get a K_0^* mass and width of 894±5 MeV and 21±3 MeV, respectively.

The next step was to cut for $M_{K\pi}$ within a 50 MeV margin of the nominal K_0^* mass. Then we combined the $K\pi$ pair with a charged kaon, calculated the invariant and 1-C fitted masses, and discarded the combinations that lay outside the invariant mass window between 1.80 and 2.10 GeV. Fig. 4.6 (I) shows the 1-C fit confidence level distribution for the surviving combinations with a fitted mass in the D_s signal
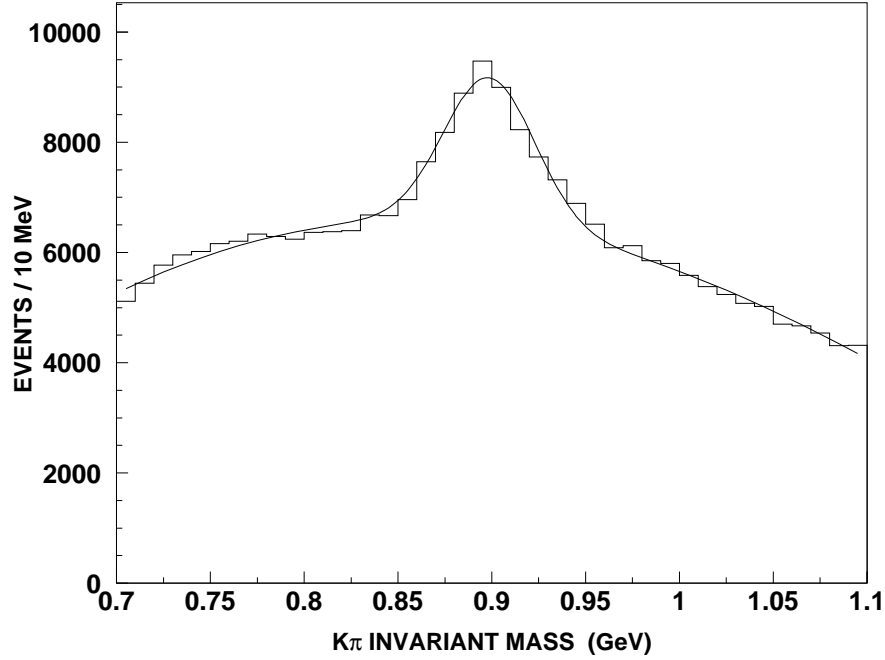
Figure 4.5: The $K^+\pi^-$ invariant mass

region. For low values of the confidence level, the distribution starts to deviate from flat, reflecting the strong non-D_s contamination. Therefore, to proceed, we required a 20% minimum confidence level for our 1-C fit. Next, we employed an additional cut in the cosine $cos\theta_{HEL}$ of the helicity angle, calculated between the secondary kaon (or pion) momentum vector in the K^* frame and the K^* momentum in the D_s frame. As in the $D_s \rightarrow \phi\pi$ case, "true" D_s decays follow a $cos^2\theta$ distribution, whereas the non-D_s distribution is essentially flat (Fig. 4.6,II,III). After requiring $|cos\theta_{HEL}| \geq 0.45$, we ended up with the final $K^{*0}K$ spectrum shown in Fig. 4.7. For comparison, we can also see the $KK\pi$ mass plot with $m_{K\pi}$ in the K^{*0} sideband (Fig. 4.8,I). No D_s enhancement is observed in the plot, indicating that the D_s signal in Fig. 4.7. is indeed a resonant $K^{*0}(892)K$ decay.
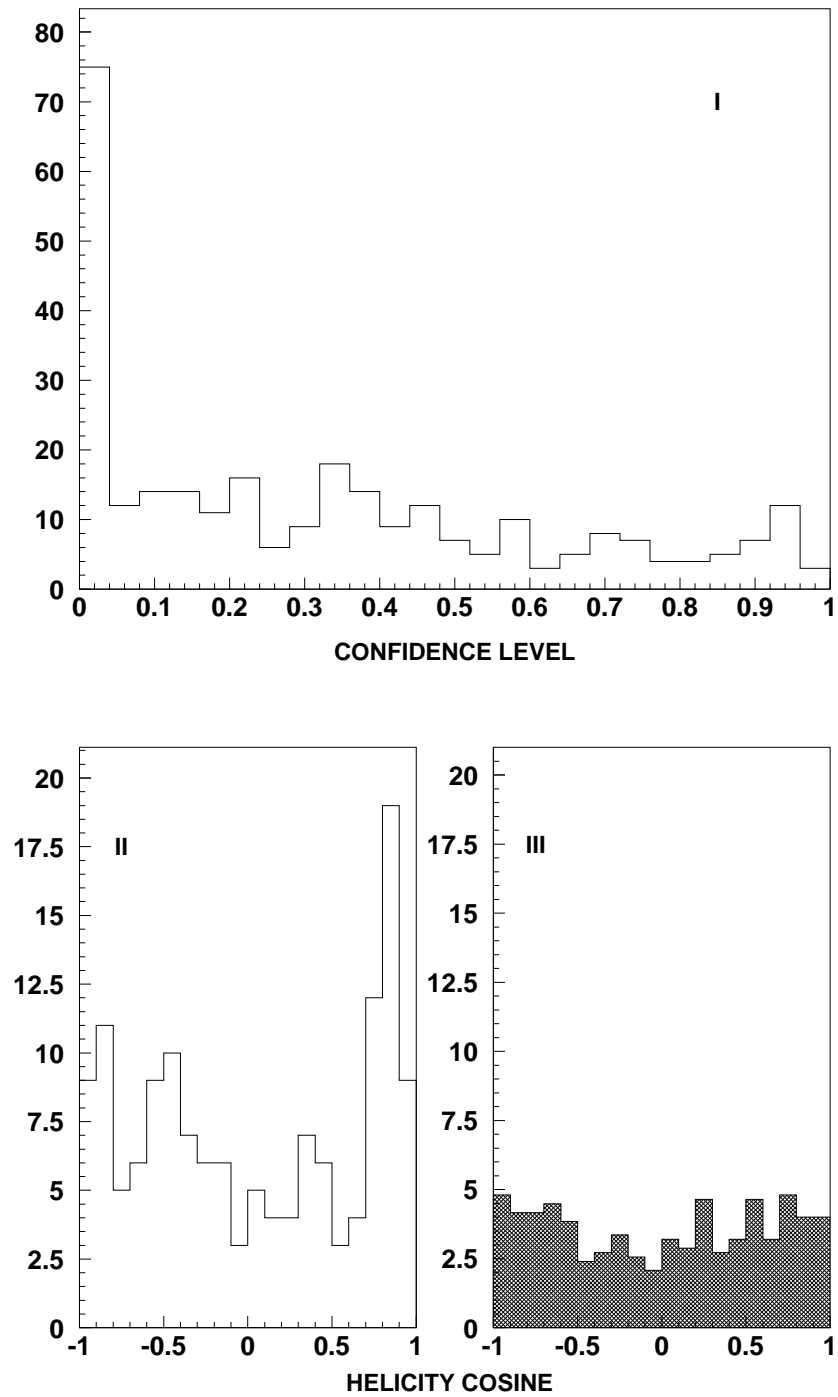
Figure 4.6: (I): The confidence level distribution for $KK\pi$ combinations in the D_s invariant mass range. (II),(III): Helicity cosine distribution for the D_s signal region (II) and sideband (III)
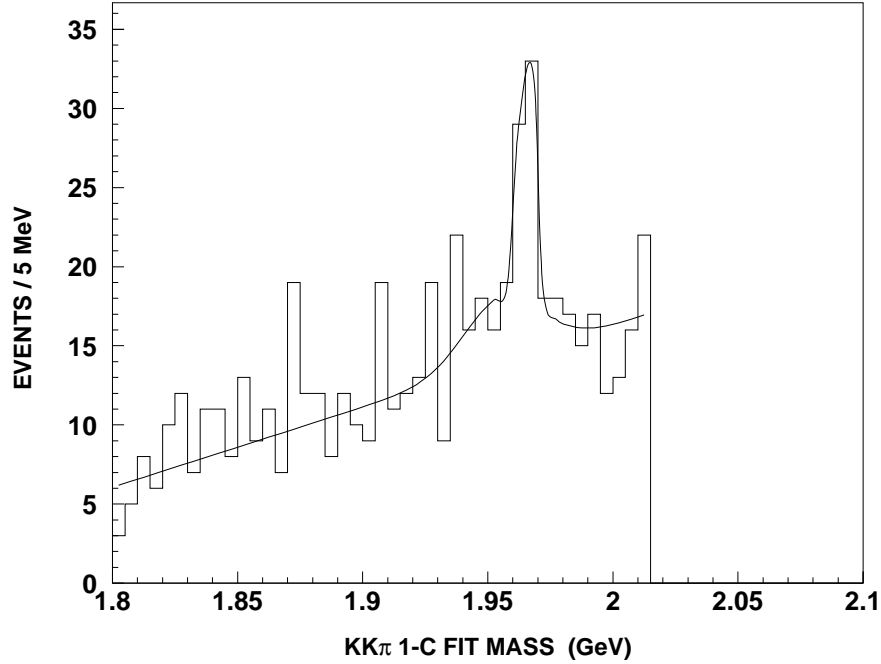
Figure 4.7: The $KK\pi$ 1-C fitted mass spectrum

Fig. 4.8(II) shows the $K^{*0}(892)K$ background, estimated from Monte Carlo simulation of the D-meson processes described in section 4.2. We can observe an enhancement in the 1.95 GeV region (mostly due to $e^+e^- \to D^*D$ with $D \to K^{*0}(892)\pi$) and a substantial number of D^*D^* combinations stacking up towards the kinematic limit. We parametrized the background of Fig. 4.7 with a simple polynomial and a wide Gaussian centered at 1.95 GeV, and obtained a signal $N_{\overline{K^{*0}}(892)K}$ of $32 \pm 9 \pm 6$ events. The systematic error is due to uncertainties in the selection criteria and the background parametrization.

The detection efficiency $\epsilon_{\overline{K^{*0}}(892)K}$ is determined by Monte Carlo to be $7.8 \pm 0.3\%$. Then we can calculate the ratio of the $\overline{K^{*0}}(892)K$ and $\phi\pi$ branching fractions:

$$\frac{\Gamma_{\overline{K^{*0}}K}}{\Gamma_{\phi\pi}} = \frac{N_{\overline{K^{*0}}K}\epsilon_{\phi\pi}}{N_{\phi\pi}\epsilon_{\overline{K^{*0}}K}} = 0.80 \pm 0.27 \pm 0.17.$$
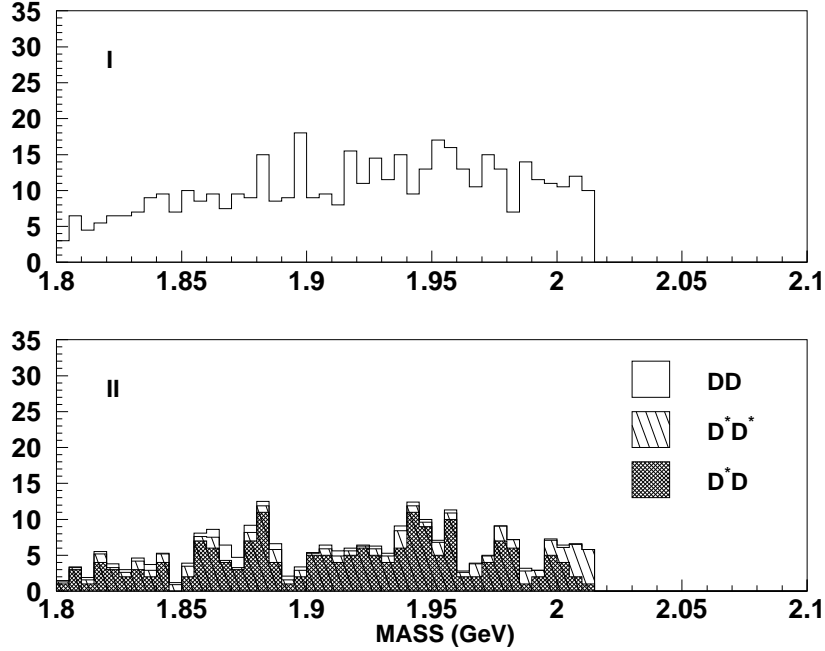
Figure 4.8: (I): the $KK\pi$ 1-C fitted mass spectrum with $K\pi$ combinations in the $K^{*0}(892)$ sideband. (II): the estimated background to the $K^{*0}(892)K$ mode.

The systematic error in the ratio gets a small additional contribution from the uncerainty in $\epsilon_{\overline{K^{*0}}(892)K}$.

4.5 $D_s \to \overline{K^0}K$; $\overline{K_s^0} \to \pi^+\pi^-$

The first step in tagging the $D_s \to \overline{K^0}K$ decay was to develop a consistent approach towards K^0 reconstruction. To this effect, we used the KLAMS package from Mark III. Given two oppositely charged tracks, with particle ID consistent with the pion hypothesis, KLAMS found their intersection (if any) in the $x - y$ plane, and re-swam the tracks to the intersection point. Then it re-calculated their projected z - positions at the vertex, as well as all relevant momenta and error matrix entries.
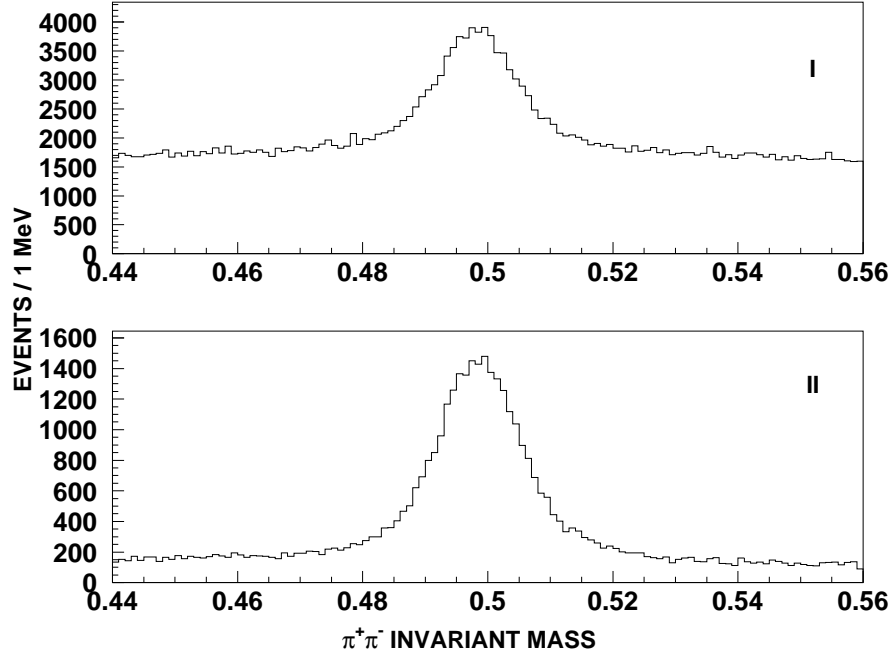
Figure 4.9: The $\pi^+\pi^-$ invariant mass, before any vertex cuts (I) and after the cuts described in section 4.5 (II).

The mass spectrum of all pions thus selected is shown in Fig. 4.9(I). Due to the relatively low momentum of the Kaons generated in the BES energy region, we could not employ a cut in the decay length R_{XY} to significantly reduce background. Fig. 4.10 shows the $\pi^+\pi^-$ invariant mass, for nine successive regions in R_{XY}:

$0 \leq R_{XY} \leq 5mm$ (region **I**)

$5 \leq R_{XY} \leq 10mm$ (region **II**)

$10 \leq R_{XY} \leq 20mm$ (region **III**)

$20 \leq R_{XY} \leq 30mm$ (region **IV**)

$30 \leq R_{XY} \leq 50mm$ (region **V**)

$50 \leq R_{XY} \leq 80mm$ (region **VI**)

$80 \leq R_{XY} \leq 120mm$ (region **VII**)

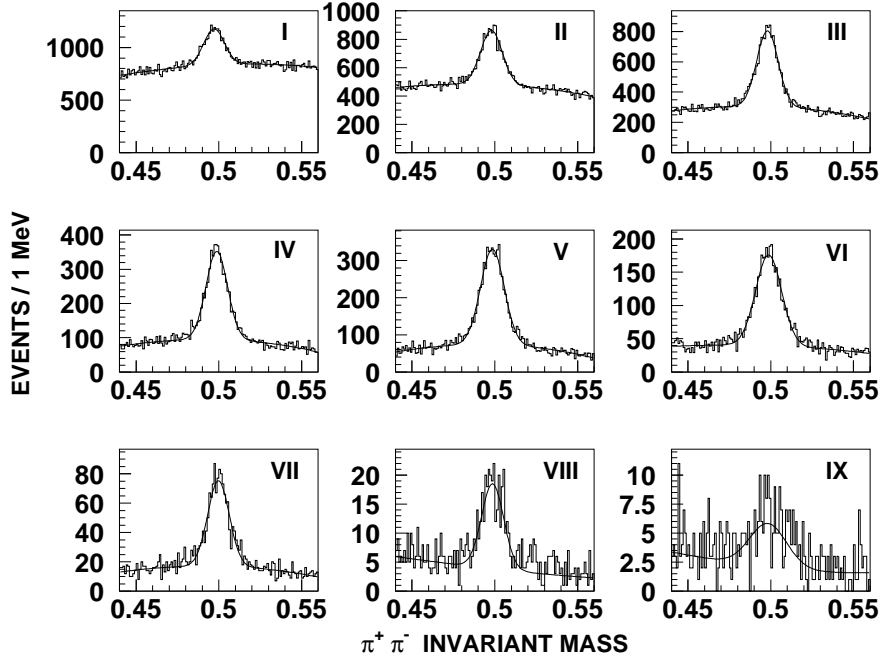$120 \leq R_{XY} \leq 160mm$ (region **VIII**)

Figure 4.10: The $\pi^+\pi^-$ invariant mass for different regions of the decay length R_{XY}. The roman numerals correspond to the intervals in R_{XY} mentioned in the text

$160 \leq R_{XY} \leq 300mm$ (region **IX**)

For all R_{XY} intervals, we can explicitly see the Signal-to-Noise (S/N) ratio and the accompanying efficiency for a corresponding R_{XY} cut (Fig. 4.11). The S/N ratio peaks at $R_{XY} \approx 40$ mm. However, the bulk of the signal lies in the shorter R_{XY} regions, and any substantial cut in R_{XY} would reduce the efficiency to unacceptably low levels. Keeping this in mind, we only employed a "soft" cut, requiring $R_{XY} \geq 7$ mm, to eliminate most of the tracks that emanate from the origin but, because of finite position resolution, fake a vertex crossing. On the other hand, the variable ξ, (the cosine of the angle in the $x - y$ plane between the reconstructed K^0 momentum vector $\vec{P}$ and the position vector $\vec{S}$ of the vertex with respect to the origin) was found very effective in reducing background (Fig. 4.12). As expected, for a "real" K^0, $\vec{P}$ is almost
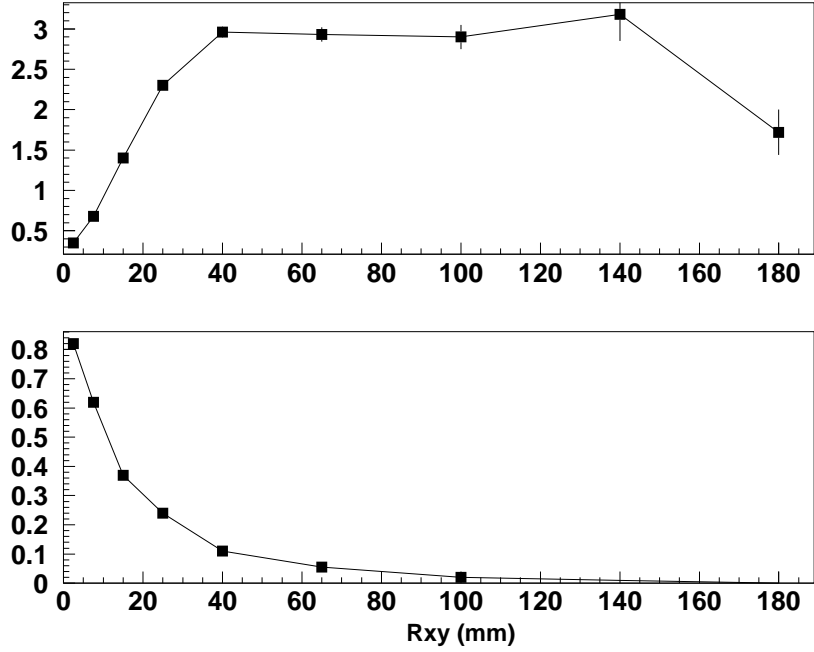
Figure 4.11: K^0 Signal-to-Noise ratio (top) and efficiency (bottom) for the different R_{XY} regions. Both quantities are normalized to the signal of Fig.4.8-I

perfectly aligned with the direction of travel $\vec{S}$; however, for an accidental crossing interpreted as a K^0, $\vec{P}$ and $\vec{S}$ can also be anti-aligned, or can have any intermediate angle between them. Another useful variable was the difference Δz between the z - positions of the tracks at the vertex. For K^0's, the distribution in $(z_1 - z_2)$ is generally narrower than that of the background. Using all the above information we employed the following set of cuts in our K^0 selection:

$$R_{XY} \geq 5mm$$

$$\xi \geq 0.95$$

$$\Delta z \leq 4cm$$

The resulting invariant mass $M_{\pi\pi}$ of all $\pi^+\pi^-$ pairs can be seen in Fig. 4.9 (bottom).
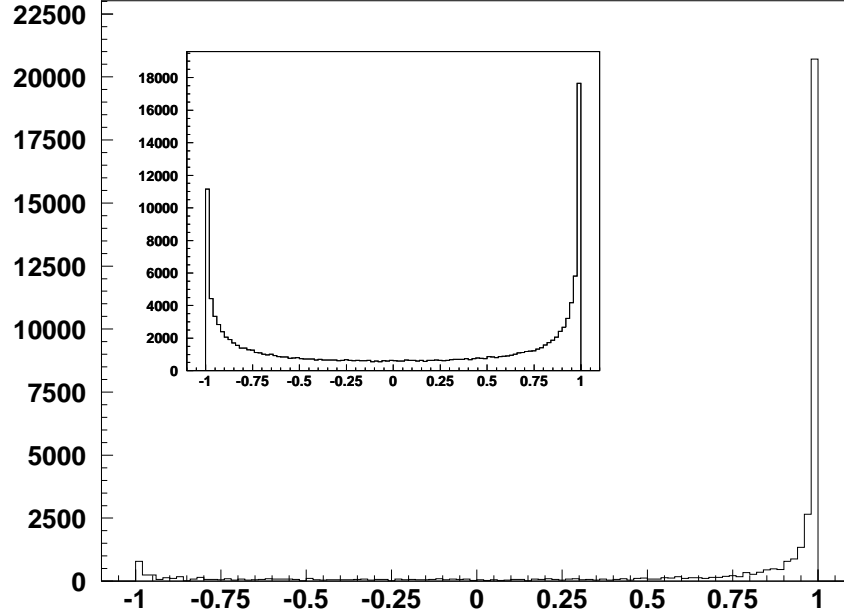
Figure 4.12: ξ, as defined in the text, for the K^0 signal (after sideband subtraction) and for the non-K^0 sideband (insert)

Next, we combined the pion pairs that satisfied $|M_{\pi\pi} - M_{K^0}| \leq 20~MeV$ with a kaon, to form the $\pi\pi K$ invariant mass and fitted mass. Since, however, the theoretical width of the K^0 is negligible, we performed a 2-constraint (2-C) kinematic fit, requiring the two-pions fitted mass to be exactly that of the K^0. To help reduce background, we required the normalized kaon likelihood to be greater that 0.8 (not 0.5, as in all other cases), and we imposed a 10% confidence level requirement for the 2-C fit. The 2-C fitted mass of the $\pi\pi K$ combinations that satisfied the above requirements and, in addition, had $1.80 \leq M_{INV} \leq 2.1$GeV is shown in Fig. 4.13-I. The resonant structure of the non-D_s combinations in the $\pi\pi K$ mass spectrum can be reproduced, to a large extent, from the Monte Carlo simulation of the D^+D^-, DD^* and D^*D^* decays (Fig. 4.13-II). After parametrizing accordingly for the background,
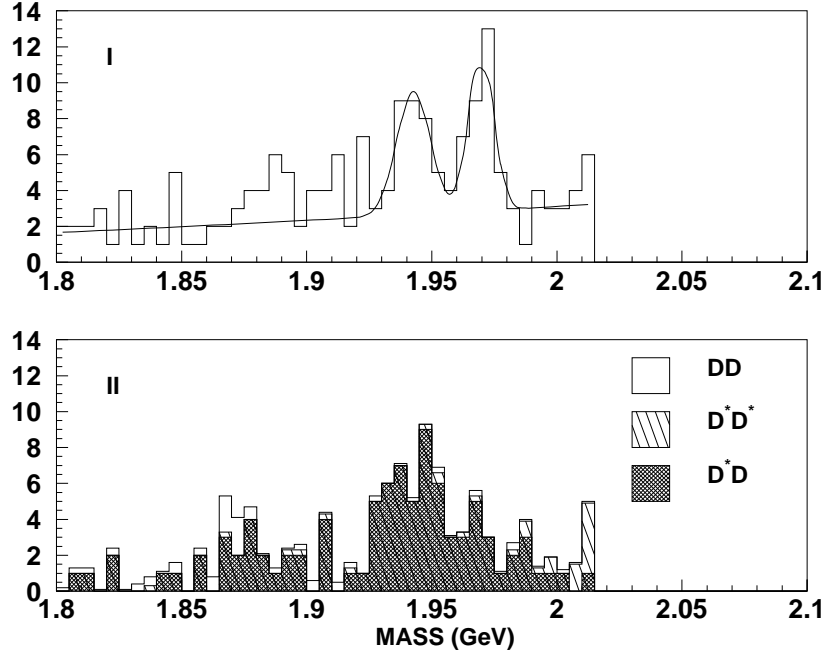
Figure 4.13: The final $K\pi\pi$ plot for data (I) and Monte Carlo generated background (II)

we got a population $N_{\overline{K^0}K}$ of $23 \pm 8 \pm 6$ events. Our efficiency was determined by the Monte Carlo to be $5.1 \pm 0.2\%$. This yields the ratio

$$\frac{\Gamma_{\overline{K^0}K}}{\Gamma_{\phi\pi}} = \frac{N_{\overline{K^0}K}\,\epsilon_{\phi\pi}}{N_{\phi\pi}\,\epsilon_{\overline{K^0}K}} = 0.88 \pm 0.29 \pm 0.25$$

The systematic error is due to uncertainties arising from the background parametrization, the selection criteria and the efficiency $\epsilon_{\overline{K^0}K}$.
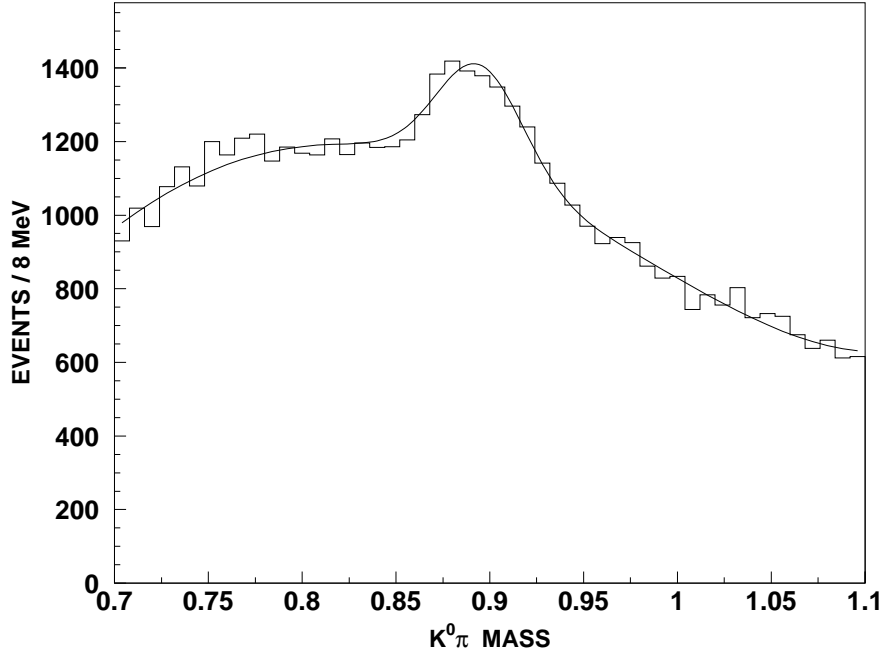
Figure 4.14: The $K^0\pi$ mass spectrum

4.6 $\;\; D_s \rightarrow \overline{K^{*0}}(892)K^*; \;\; \overline{K^{*0}}(892) \rightarrow K^-\pi^+; \;\; K^*(892) \rightarrow K^0\pi^+; \;\; K_s^0 \rightarrow \pi^+\pi^-$

We started our search for $D_s \rightarrow K^{*0}K^*$ by requiring 5 or more good charged tracks, satisfying the charge and particle ID requirements of a ($\pi^+\;\pi^-\;\pi^+$) (π^+K^-) final state. First we looped over all pion pairs to form a K^0, in the exact same manner of section 4.5. Then we combined all the pion pairs that had $m_{\pi^+\pi^-}$ within 20 MeV of the nominal K^0 mass with a third pion, to look for the charged $K^*(892)$ (Fig. 4.14). Finally, we looped over the remaining $K^-\pi^+$ combinations to look for $K^{*0}(892)$'s (as in section 4.4).

In this particular mode, we had two intermediate resonances (instead of one). We required both the K^* and the K^{*0} candidate masses to be within 100 MeV of the
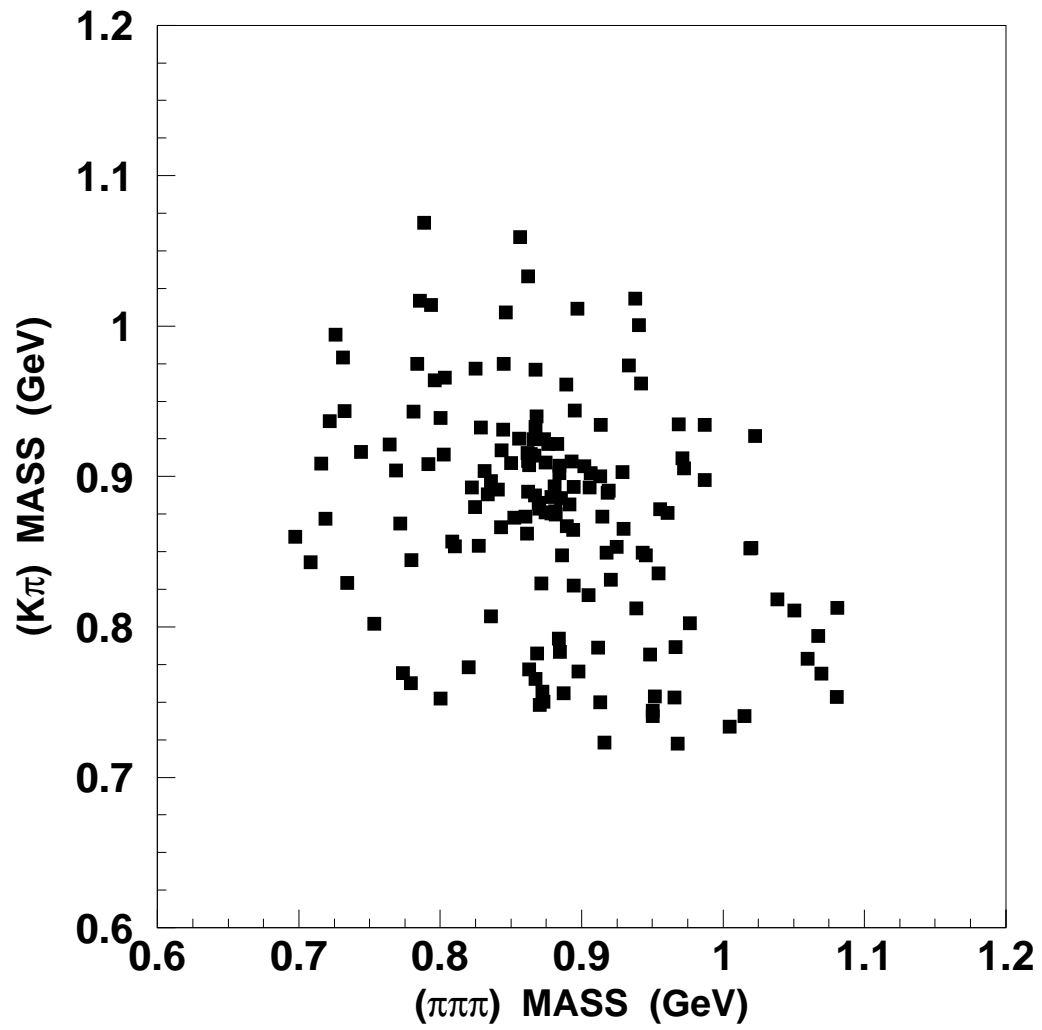
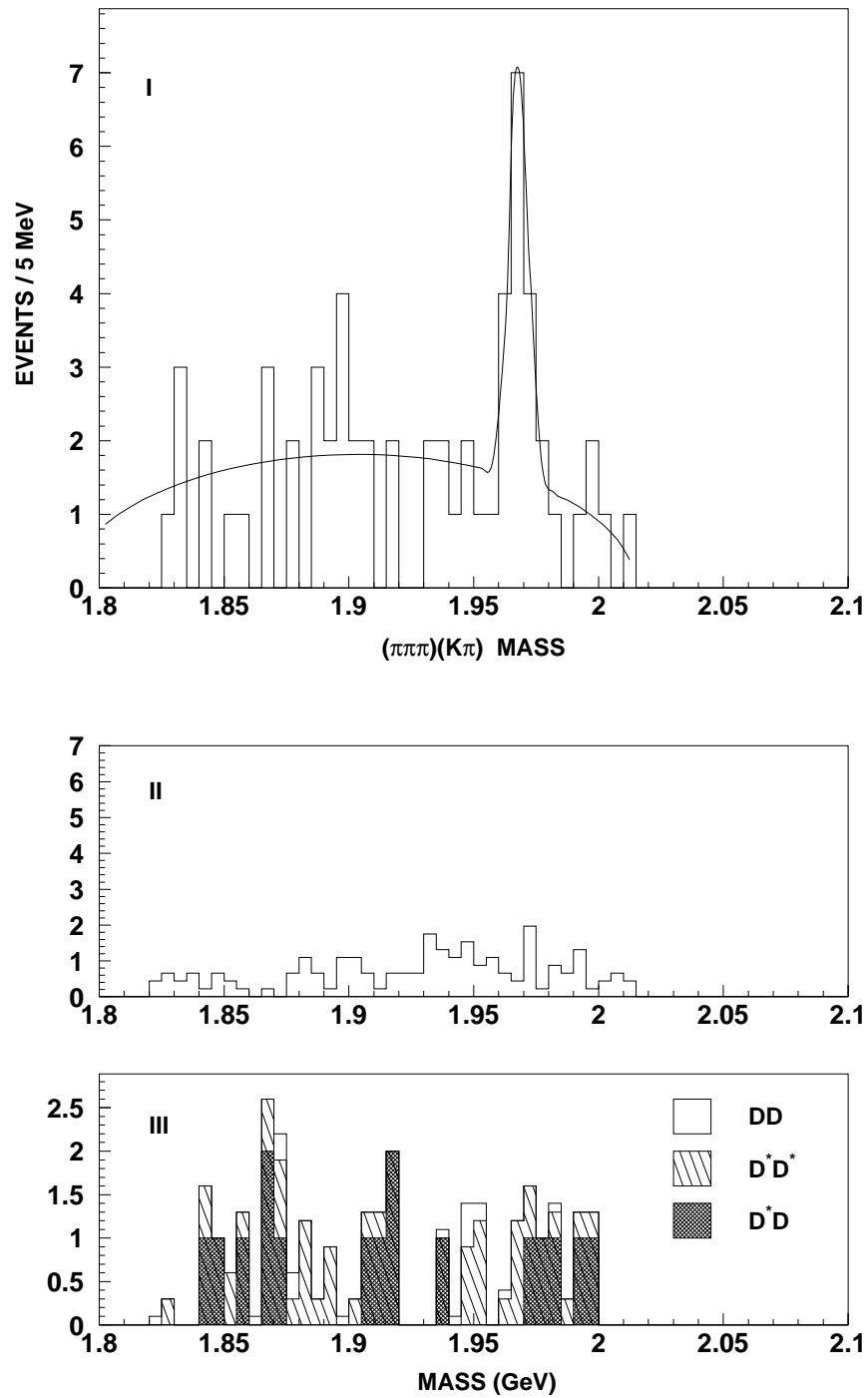Figure 4.15: $K\pi$ mass against $K^0\pi$ mass for Monte Carlo events

Figure 4.16: $K^{*0}K^*$ 2-C fitted mass spectrum (I). The same plot for combinations in the K^* sidebands (II) and for Monte Carlo background (III)

nominal ones. Then, after verifying from Monte Carlo events that the K^* and K^{*0} masses were distributed in an uncorrelated fashion (Fig. 4.15) we built a generalized χ^2 of the form:

$$\chi^2 = \Big(\frac{m_{K^0\pi} - m_{K^*(892)}}{\sigma_{K^*}}\Big)^2 + \Big(\frac{m_{K\pi} - m_{K^{*0}(892)}}{\sigma_{K^{*0}}}\Big)^2$$

where the mass resolution σ was taken to be the half-width of the $K^*(892)$, or about 23 MeV. For each combination, we turned the χ^2 value into a confidence level (CL), and then cut at CL$\geq$10%. The combinations that survived were subjected to a 2-C kinematic fit (as in the K^0K mode, the K^0 candidate tracks were constrained on the K^0 mass) with a 10% confidence level cut. Fig. 4.16 shows the fitted mass of the events that satisfied the 2-C fit criteria. We see a clear enhancement in the D_s region, containing $11 \pm 4 \pm 2.5$ events over a phase space background. Again, the systematic error reflects uncertainties in the selection criteria and background parametrization. For comparison, we can also see the mass plot for combinations in the sidebands of K^* or K^{*0} (or both), as well as the plot for the (estimated) background to the K^*K^{*0} mode. No enhancement in the D_s region is seen in either case.

The detection efficiency for $D_s \to K^*K^{*0}$ is determined by Monte Carlo at $1.6 \pm 0.1\%$. This yields the ratio

$$\frac{\Gamma_{\overline{K^{*0}}K^*}}{\Gamma_{\phi\pi}} = \frac{N_{\overline{K^{*0}}K^*}\,\epsilon_{\phi\pi}}{N_{\phi\pi}\,\epsilon_{\overline{K^{*0}}K^*}} = 1.34 \pm 0.56 \pm 0.34$$

As in the previous modes, there is an additional contribution to the systematic error due to the uncertainty in the efficiency.

4.7 Conclusions

In this chapter, I presented our analysis of inclusive (or "single tag") D_s decays. We observe a clear D_s signal in the following four modes:

- $D_s \to \phi\pi;\ \phi \to K^+K^-$

- $D_s \to \overline{K^{*0}}(892)K;\ \overline{K^{*0}}(892) \to K^-\pi^+$
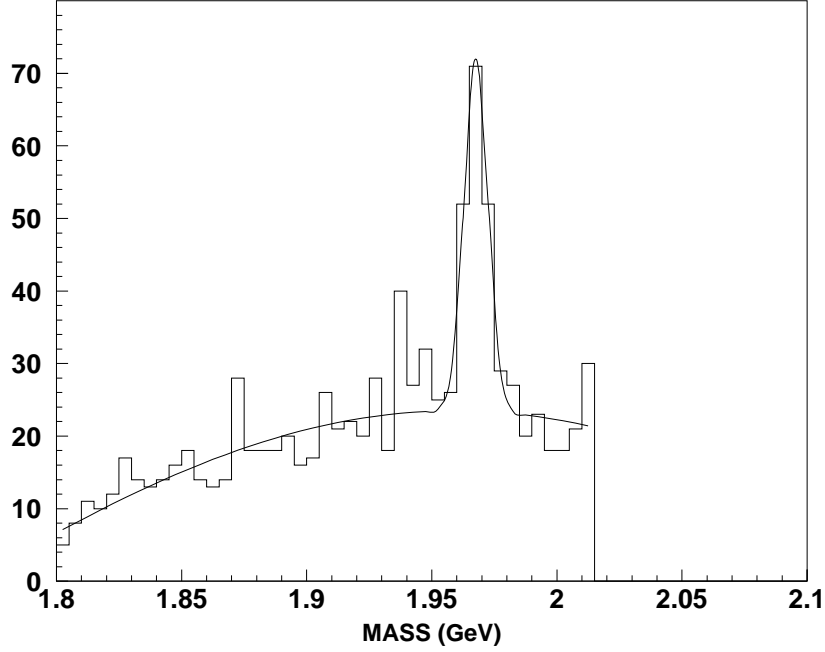
Figure 4.17: The D_s signal from all four modes described in this chapter

- $D_s \to \overline{K^0}K$; $\overline{K_s^0} \to \pi^+\pi^-$

- $D_s \to \overline{K^{*0}}(892)K^*$; $\overline{K^{*0}}(892) \to K^-\pi^+$; $K^*(892) \to K^0\pi^+$; $K_s^0 \to \pi^+\pi^-$

The D_s signal from the above four modes combined can be seen in Fig. 4.17. The peak contains $106 \pm 16 \pm 15$ events. The quantity $\sigma_{D_s^+D_s^-} \cdot Br_{\phi\pi}$ was calculated to be:

$$\left(\sigma_{e^+e^- \to D_s^+D_s^-}\right) \cdot \left(Br_{D_s \to \phi\pi}\right) = 11.1 \pm 1.8 \pm 1.0 \,\text{pb}.$$

If we consider only the $\phi\pi$ mode, and assume the world average value for $Br_{D_s \to \phi\pi}$ of $3.5\pm0.4\%$, we find the $D_s^+D_s^-$ production cross-section at 4.03 GeV to be:

$$\sigma_{e^+e^- \to D_s^+D_s^-} = 317 \pm 52 \pm 47 \,\text{pb}.$$

The $\phi\pi$ signal also gives a D_s mass of 1968.2 ± 0.9 MeV, in good agreement with the world average of 1968.5 ± 0.7 MeV.

Chapter 5

Analysis: D_s double tag decays ; $Br_{D_s \to \phi\pi}$

5.1 Double Tag Event Selection

This chapter will describe the search for fully reconstructed, exclusive (or "double tag") D_s decays. As was mentioned in the Introduction, we used the method of double tagging to get a model-independent estimate for $Br_{D_s \to \phi\pi}$. Our double tag candidate set consisted of events in which both D_s mesons decayed through one of the four modes described in Chapter 4: $\phi\pi$, $\overline{K^0}K$, $\overline{K^{*0}}(892)K$ and $\overline{K^{*0}}(892)K^*$. A summary of all candidate final states, accompanied by their respective detection efficiencies, can be seen in Table 5.1.

We started our search by selecting charge balanced events with the correct number of charged tracks (i.e. six, eight or ten – see Table 5.1), no isolated photons, and particle ID assignments consistent with the detected final state. Since the background is much smaller for double tags than it is for single tags, we did not use a cut in the Kaon likelihood, but simply imposed a confidence level requirement

$$CL^{K/\pi} \geq 0.01$$

to select both pions and kaons.

Next, we subjected all the candidates to a 5-constraint (5-C) kinematic fit. We

mode 1	mode 2	efficiency	N_{TRACKS}
$D_s \to \phi\pi$	$D_s \to \phi\pi$	2.05%	6
$D_s \to \phi\pi$	$D_s \to \overline{K^0}K$	1.91%	6
$D_s \to \phi\pi$	$D_s \to \overline{K^{*0}}K$	2.20%	6
$D_s \to \phi\pi$	$D_s \to \overline{K^{*0}}K^*$	0.23%	8
$D_s \to \overline{K^0}K$	$D_s \to \overline{K^0}K$	2.11%	6
$D_s \to \overline{K^0}K$	$D_s \to \overline{K^{*0}}K$	2.25%	6
$D_s \to \overline{K^0}K$	$D_s \to \overline{K^{*0}}K^*$	0.20%	8
$D_s \to \overline{K^{*0}}K$	$D_s \to \overline{K^{*0}}K$	3.20%	6
$D_s \to \overline{K^{*0}}K$	$D_s \to \overline{K^{*0}}K^*$	0.31%	8
$D_s \to \overline{K^{*0}}K^*$	$D_s \to \overline{K^{*0}}K^*$	0.02%	10

Table 5.1: Exclusive final states and associated efficiencies. N_{TRACKS} is the detected number of tracks for each final state

imposed conservation of energy and momentum (4 constraints), together with the requirement, also used in the single tag search, that each D_s candidate in the event recoils against an equal (but unspecified) mass. We required the χ^2 of the fit to correspond to a confidence level $CL \geq 0.01$. Finally, we employed the same intermediate mass cuts that we used in our single-tag search:

- $|m_{K^+K^-} - m_\phi| \leq 15 MeV$

- $|m_{\pi^+\pi^-} - m_{K^0}| \leq 20 MeV$

- $|m_{K^+\pi^-} - m_{K^{*0}}| \leq 50 MeV$, and

- $CL(m_{K^0\pi^+}, m_{K^+\pi^-}) \geq 0.1$, for the K^*K^{*0} mode (see section 4.6)

After applying these selection criteria to the entire data sample, we came up with two double-tag events, shown in table 5.2. No other candidate event enters the signal region $1.8 \leq m \leq 2.1 GeV$. Fig. 5.1 shows the two double tag events in cross-sectional
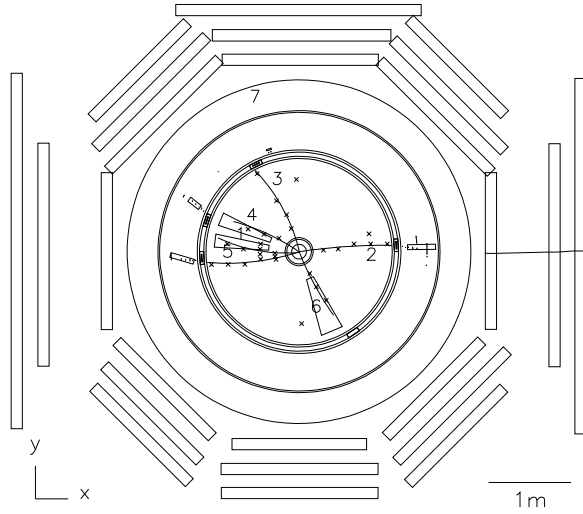
Run   4838
Event 11178

M_{Fit} 1.968 MeV

$D_S \to \phi\pi$
M_ϕ 1.013 MeV
M_{Inv} 1.952 MeV
M_{BC} 1.970 MeV
Tracks 4, 1, 6

$D_S \to K^{*0}K$
M_{K^*} 0.855 MeV
M_{Inv} 2.013 MeV
M_{BC} 1.955 MeV
Tracks 3, 2, 5
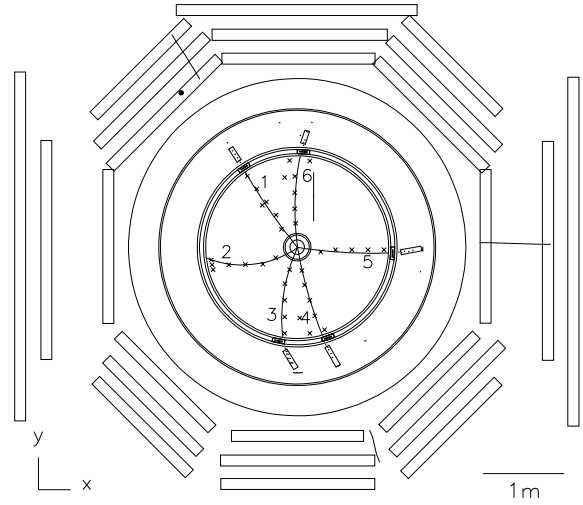
Run   6422
Event 27143

M_{Fit} 1.968 MeV

$D_S \to K^{*0}K$
M_{K^*} 0.879 MeV
M_{Inv} 1.988 MeV
M_{BC} 1.965 MeV
Tracks 5, 1, 2

$D_S \to K^{*0}K$
M_{K^*} 0.913 MeV
M_{Inv} 1.951 MeV
M_{BC} 1.962 MeV
Tracks 6, 4, 3

Figure 5.1: Cross-section displays of the two double-tag events shown in Table 5.2. M_{BC} refers to the "beam constrained mass" $\equiv ((E_{beam}/2)^2 + |\sum \vec{P}|^2)^{1/2}$

mode 1	mode 2	$M_{INV}1$	$M_{INV}2$	M_{FIT}
$D_s \to \phi\pi$	$D_s \to \overline{K^{*0}}K$	1.952 GeV	2.013 GeV	1.968 GeV
$D_s \to \overline{K^{*0}}K$	$D_s \to \overline{K^{*0}}K$	1.988 GeV	1.951 GeV	1.968 GeV

Table 5.2: D_s double tag candidates

view. Each event contains six charged tracks, without any photons registering in the shower counter.

To estimate the double tag background, we have to consider both resonant and continuum contributions. We estimated the continuum contribution to be ~ 0.1 event, by normalizing the background population of Fig 5.2 to an area corresponding to $\sim 2\sigma$ from the D_s mass in both modes. For an estimate of the resonant contribution, we generated a total 1.6 million events (or, roughly, the equivalent to 10 times our data sample) in the modes $e^+e^- \to D\overline{D}$, $e^+e^- \to D^*D$, $e^+e^- \to D^*D^*$. One event satisfied all our selection criteria, giving us a total background estimate of $N^{bg}_{DT} = 0.2 \pm 0.2$ events.

To check the validity of the 5-C fit procedure, we performed an independent search, using the unfitted track momenta. We required the total measured momentum of the combination to be less than 100 MeV. Furthermore, we required the energy for each candidate D_s combination to lie within four standard deviations from the nominal value of $\sqrt{s}/2$. After we applied these search criteria to the whole data sample, we ended up with the same two double-tag events selected through the kinematic fit procedure. No other candidates were found within 3σ of the nominal mass for each D_s (see Fig . 5.2).
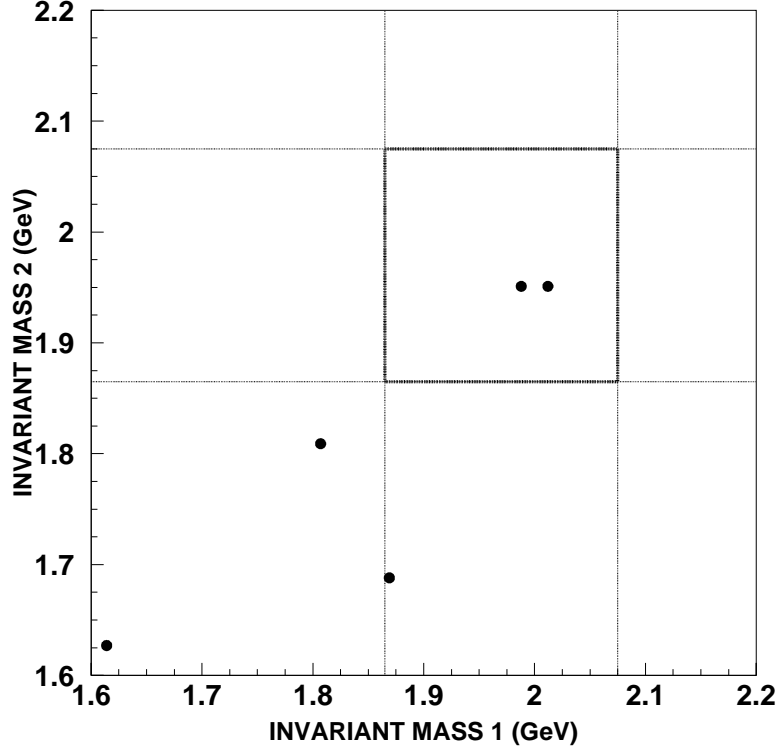
Figure 5.2: Invariant mass of mode 1 vs. mode 2 for double tag candidates selected without kinematic fitting. The dotted lines correspond to a 3σ interval for the two masses around the D_s mass

5.2 Determination of $Br_{D_s \to \phi\pi}$

5.2.1 Likelihood Method and Statistical Error

To determine $Br_{D_s \to \phi\pi}$ we use the general formula outlined in Sect. 1.6.

$$Br_{D_s \to \phi\pi} = 2 \cdot \frac{N_{DT}}{N_{ST}} \cdot \frac{\sum_i^n b_i \epsilon_i}{\sum_{i,j}^n b_i b_j \epsilon_{ij}}$$

b_i and ϵ_i are the relative branching fraction $\Gamma_i / \Gamma_{\phi\pi}$ and the single tag detection efficiency of the ith mode, and ϵ_{ij} is the double tag detection efficiency for the final

state i vs. j. (All efficiency figures refer to the 5-C fit search method, and the the branching ratios B_i are taken from the Particle Data Group). N_{DT} is the "true" number of double dags:

$$N_{DT} = N_{DT}^{observed} - N_{DT}^{bg}$$

where N_{DT}^{bg} denotes the number of expected background events. N_{ST} is the number of observed single tag events, which, for the purposes of this calculation is taken to be:

$$N_{ST} = \frac{N_{\phi\pi}}{\epsilon_{\phi\pi}} \sum_i \epsilon_i b_i.$$

The reason we normalize to $\phi\pi$ is that this is by far the cleanest and best measured mode in our data. Combining the above formulas, we get:

$$Br_{D_s \to \phi\pi} = \frac{N_{DT}}{N_{\phi\pi} \cdot \kappa}$$

where we define

$$\kappa \equiv \frac{\sum_{i,j} b_i b_j \epsilon_{ij}}{2\epsilon_{\phi\pi}} \simeq 1.23 \pm 0.05$$

The error is due to uncertainties in the detection efficiency and the branching fractions b_i.

To assign a central value and a statistical error to $B_{\phi\pi}$, we build a likelihood function that combines the information from both our single tag and our double tag signal:

$$\mathcal{L}(N_{\phi\pi}, B_{\phi\pi}) = e^{(-N_{DT})} \left[\frac{(N_{DT})^{n_{DT}}}{n_{DT}!} \right] \left[\frac{1}{\sigma(n_{\phi\pi})\sqrt{2\pi}} e^{-\frac{(n_{\phi\pi} - N_{\phi\pi})^2}{2\sigma^2(n_{\phi\pi})}} \right]$$

Here $n_{\phi\pi,DT}$ is the observed $\phi\pi$ and double tag signal; $\sigma(n_{\phi\pi})$ denotes the statistical error to $n_{\phi\pi}$, which is assumed Gaussian distributed. Then $\mathcal{L}(N_{\phi\pi}, B_{\phi\pi})$ simply denotes the probabilty that an *actual* population of $N_{\phi\pi}$, N_{DT} will fluctuate to an *observed* signal $n_{\phi\pi}$, n_{DT}; the $B_{\phi\pi}$ dependence of $\mathcal{L}$ comes through the equation $Br_{\phi\pi} = N_{DT}/(N_{\phi\pi} \cdot \kappa)$. Next, for each value of $B_{\phi\pi}$ we integrated $\mathcal{L}$ to get the "marginalized" likelihood for $B_{\phi\pi}$:

$$\mathcal{L}_m(B_{\phi\pi}) = \int_0^\infty \mathcal{L}(B_{\phi\pi}, N_{\phi\pi}) d(N_{\phi\pi})$$

The plot of $\mathcal{L}$ for different values of $B_{\phi\pi}$ can be seen in Fig. 5.3. $\mathcal{L}_m$ is maximum for
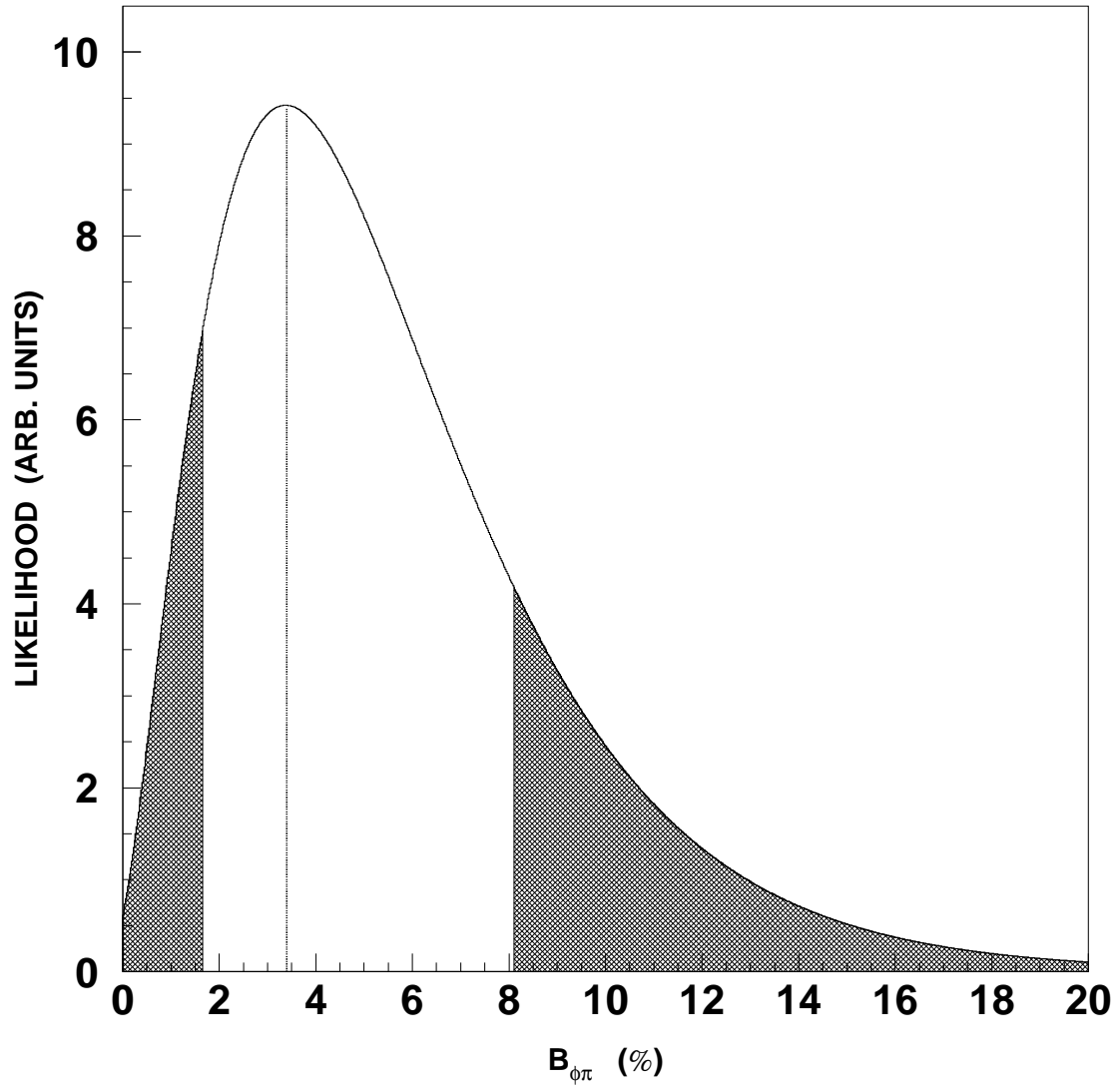
Figure 5.3: Marginalized likelihood for $B_{\phi\pi}$

$B_{\phi\pi} = 3.4\%$ The high (low) shaded region corresponds to a $\pm 1\sigma$ (or 68.3% inclusion) above (below) the peak. Summarizing, thus far, we get:

$$B_{\phi\pi} = 3.4^{+4.8}_{-1.7}\%$$

5.2.2 Systematic Errors

The largest contribution to the systematic error (roughly $^{+1.2}_{-0.3}$) comes from variations in the double tag selection criteria. Widely varying sets of cuts left the double tag signal unchanged, while substantially changing the detection efficiency. The double tag signal was insensitive to cuts in helicity angle, K^0 vertexing parameters, and particle ID normalized likelihoods. (The two events even satisfied the stringent requirement $\mathcal{L}^{K/\pi}_{normalized} \geq 0.5$ for all six tracks). The signal was also left unchanged after a 1σ relaxation in the intermediate mass cuts. Other sizeable contributions were due to the systematic error in determining $N_{\phi\pi}$ ($^{+0.4}_{-0.4}$), and the uncertainties in κ ($^{+0.1}_{-0.1}$) and N^{bg}_{DT} ($^{+0.4}_{-0.4}$). In view of these estimates, our result for $B_{\phi\pi}$ becomes

$$Br_{D_s \to \phi\pi} = 3.4^{+4.8+1.3}_{-1.7-0.7}\%$$

This value is consistent with the present world average of $3.5 \pm 0.4\%$.

5.3 Conclusion

In this chapter I presented our search for exclusive (or "double tag") D_s decays. We looked for events in which both candidate D_s mesons decayed into one of the following modes: $\phi\pi$, $\overline{K^0}K$, $\overline{K^{*0}}(892)K$ and $\overline{K^{*0}}(892)K^*$.

Two such events were found. In conjunction with our single tag measurements, this yields a model-independent estimate of the Branching fraction for $D_s \to \phi\pi$:

$$Br_{D_s \to \phi\pi} = 3.4^{+4.8+1.3}_{-1.7-0.7}\%$$

This value is consistent with the present world average of $3.5 \pm 0.4\%$.

5.4   Future prospects

The error in our determination of $B_{\phi\pi}$ is mostly due to our limited double-tag statistics. With the present data set, these statistics could be improved through the inclusion of other prominent modes, namely $\eta\pi$ and $\eta\prime\pi$.

For the near future (after the 1995 data taking period) a major upgrade is planned for both BES and BEPC. The BEPC upgrade will increase the luminosity by a factor of ~ 4. BES will install a new drift chamber, a vertex chamber, and an improved set of Time of Flight counters. The ToF resolution for the new set of counters is expected to be ~ 220ps, allowing a $3\sigma K/\pi$ separation for momenta up to 800 GeV. The vertex chamber will increase our secondary vertex detection capability, and the new drift chamber will allow for a better momentum resolution. The drift chamber code will be re-written to allow for better reconstruction of close-lying tracks and (possibly) for partial detection of charged Kaons decaying inside the drift chamber. In all, improvements in the software and the hardware are expected to increase our double-tag detection efficiency by about 50%. Consequently, a year's worth of consistent running in the upgraded BES/BEPC could yield a measurement of $Br_{D_s \to \phi\pi}$ with an error at the level of 25%.

Appendix A

Spin Transformations and the Helicity Angle

The following is a brief discussion on the relativistic transformations of spin and helicity eigenstates. It generally follows the presentation of Suh Urk Chung [32] and the definitions of Rose [33], and will help the reader understand the "helicity angle cosine' distributions mentioned in Sections 4.3 and 4.4.

If the vector $|jm\rangle$ is the canonical representation of the state with spin j and spin z-component m, then the unitary operator corresponding to the rotation $R(\alpha, \beta, \gamma)$ of the physical system around the Euler angles α, β and γ can be written as:

$$U[R(\alpha, \beta, \gamma)] = e^{-i\alpha J_z} e^{-i\beta J_y} e^{-i\gamma J_z}$$

The rotated state is given by:

$$U[R(\alpha, \beta, \gamma)]|jm\rangle = \sum_{m'} |jm'\rangle D^j_{m'm}(\alpha, \beta, \gamma)$$

where $D^j_{m'm}$ is the standard rotation matrix

$$D^j_{m'm}(\alpha, \beta, \gamma) = \langle jm'|U[R(\alpha, \beta, \gamma)]|jm\rangle$$

$$= e^{-im'\alpha} d^j_{m'm}(\beta) e^{-im\gamma}$$

and the d-function is defined as:

$$d^j_{m'm}(\beta) = \langle jm'|e^{-i\beta J_y}|jm\rangle$$

The most general unitary transformation of the state $|jm\rangle$ can be represented by a sequence of rotations and/or pure Lorentz transformations along the quantization axis. If we denote the the pure Lorentz transformation along the quantization (z) axis as $L_z(|\vec{p}|)$, then a general Lorentz boost along $\vec{p}$ (with direction angles ϑ, φ) is given by:

$$L(\vec{p}) = R(\vartheta, \varphi, 0)L_z(|\vec{p}|)R^{-1}(\vartheta, \varphi, 0)$$

leading to the operator relation:

$$U[L(\vec{p})] = U[R(\vartheta, \varphi, 0)]U[L_z(|\vec{p}|)]U^{-1}[R(\vartheta, \varphi, 0)]$$

Then a canonical state describing a single particle with spin j and momentum $\vec{p}$ is defined as:

$$|\vec{p}, jm\rangle = U[R(\vartheta, \varphi, 0)]U[L_z(|\vec{p}|)]U^{-1}[R(\vartheta, \varphi, 0)]|jm\rangle$$

Similarly, we can define a *helicity* state $|\vec{p}, j\lambda\rangle$ through the transformation property:

$$|\pm\vec{p}, j\lambda\rangle = U[R(\vartheta, \varphi, 0)]U[L_{\pm z}(|\vec{p}|)]|j\lambda\rangle$$

To investigate the helicity distributions of the decays $|JM\rangle \rightarrow (1)(2)$ we must be able to construct states of definite angular momentum out of helicity eigenstates. A two-particle state with net momentum $|\vec{p}| = 0$ and individual helicities λ_1 and λ_2 can be represented by:

$$|\varphi\vartheta\lambda_1\lambda_2\rangle = U[R(\vartheta, \varphi, 0)](U[L_z(|\vec{p}|)]|s_1\lambda_1\rangle U[L_{-z}(|\vec{p}|)]|s_2\lambda_2\rangle)$$

where the angles φ, ϑ characterize the momentum axis, and $|s_i\lambda_i\rangle$ refers to the spin and helicity of the ith particle. We have assumed the particles are not identical, and ignored the normalization constant. The decomposition of an angular momentum eigenstate $|JM\lambda_1\lambda_2\rangle$ into plane wave states $|\varphi\vartheta\lambda_1\lambda_2\rangle$ can be derived from first principles [34], but is given here without proof:

$$|JM\lambda_1\lambda_2\rangle \propto \int d\Omega D_{M\lambda}^{J*}(\varphi, \vartheta, \lambda_1\lambda_2)|\varphi\vartheta\lambda_1\lambda_2\rangle$$

where $\lambda = \lambda_1 - \lambda_2$ and $d\Omega = d\varphi\, d\cos\vartheta$. We can always verify that, expanded in this manner, $|JM\lambda_1\lambda_2\rangle$ satisfies the rotation transformation

$$U[R']|JM\lambda_1\lambda_2\rangle = \sum_{M'} D_{MM'}^J|JM'\lambda_1\lambda_2\rangle$$

as required from angular momentum eigenstates. If we adopt the normalization

$$\langle \Omega' \lambda_1{}' \lambda_2{}' | \Omega \lambda_1 \lambda_2 \rangle = \delta^{(2)}(\Omega - \Omega') \delta_{\lambda_1 \lambda_1'} \delta_{\lambda_2 \lambda_2'}$$

we obtain the relation

$$\langle \Omega' \lambda_1{}' \lambda_2{}' | J M \lambda_1 \lambda_2 \rangle \propto D_{M\lambda}^{J*}(\varphi, \vartheta, 0) \delta_{\lambda_1 \lambda_1'} \delta_{\lambda_2 \lambda_2'}$$

The angular distribution of $|JM\rangle \to (1)(2)$ can then be derived as follows:

$$d\sigma/d\Omega = \langle \Omega \lambda_1 \lambda_2 | \mathcal{M} | JM \rangle$$

$$= \langle \Omega \lambda_1 \lambda_2 | \left(\sum_{J', M', \lambda_1' \lambda_2'} |J', M', \lambda_1' \lambda_2'\rangle \langle J', M', \lambda_1' \lambda_2'| \right) | \mathcal{M} | JM \rangle$$

where we used the completeness of the $|JM\lambda_1\lambda_2\rangle$ set. Finally, the normalization relations and angular momentum conservation reduce the summation to:

$$d\sigma/d\Omega \propto \langle \Omega \lambda_1 \lambda_2 | | J M \lambda_1 \lambda_2 \rangle \langle J M \lambda_1 \lambda_2 | | \mathcal{M} | JM \rangle$$

$$\propto F_{M\lambda}^{J} D_{M\lambda}^{J*}(\varphi, \vartheta, 0)$$

The "F" factor is the *helicity decay amplitude* $\langle J M \lambda_1 \lambda_2 | \mathcal{M} | JM \rangle$; it only depends on rotationally invariant quantities (J, λ_1, λ_2), and is not a function of the ϑ, φ coordinates. Therefore, all dependence of the differential cross-section on ϑ, φ is included in the D - function.

In the decay $D_s \to \phi\pi$ (or, equivalently, $D_s \to K^{*0}K$), the D_s has no intrinsic angular momentum. Since the orbital angular momentum of the $\phi\pi$ pair has no component along the direction of the tracks, angular momentum conservation in the D_s rest frame implies that, if we use the direction of the $\phi\pi$ pair as our quantization axis, the ϕ particle is a pure $|1, 0\rangle$ state. Then for the decay $\phi \to K^+K^-$ (or $K^{*0} \to K^+\pi^-$), we observe that the resulting K's and π's have intrinsic angular momentum (and, hence, helicity) equal to zero. Then the decay amplitude for the ϕ (or K^{*0}) decay is given by

$$A \propto D_{00}^{1*} \propto \cos \vartheta$$

Then the differential cross-section is proprtional to $|A|^2 \propto \cos^2 \vartheta$, where the angle is defined between the ϕ (or K^{*0}) momentum and the momentum axis of the decay products in the ϕ (or K^{*0}) reference frame.

Bibliography

[1] M. Gell-Mann, Phys. Rev. **92**, 833 (1953)

[2] T. Nakano, K. Nishijima, Prog. Theor. Phys. (Kyoto) **10**, 581 (1955)

[3] M. Gell-Mann, Phys. Lett. **8**, 214 (1964)

[4] S.L. Glashow, Nucl. Phys. **22**, 579 (1961)

[5] S. Weinberg, Phys. Rev. Lett. **19**, 1264 (1967)

[6] A. Salam, *Elementary Particle Theory: Relativistic Groups and Analyticity* (Nobel Symposium No. 8) ed. by N. Svartholm, Almqvist and Wiksell, Stockholm, 1968, p. 367.

[7] S.L. Glashow, J. Iliopoulos, L. Maiani, Phys.Rev. **D 2**, 1285 (1970)

[8] J.E. Augustin *et al.*, Phys. Rev Lett. **33**, 1406 (1974)

[9] J.J. Aubert *et al.*, Phys. Rev Lett. **33**, 1404 (1974)

[10] E. Fermi, Ric. Sci. **4**, 491 (1933)

[11] N. Cabibo, Phys. Rev. Lett. **10**, 531 (1963)

[12] M. Kobayashi, T. Maskawa, Prog. Theoret. Phys. (Kyoto) **49**, 652 (1973)

[13] E. Eichten *et al.*, Phys. Rev. **D 21**, 203 (1980)

[13] W.S. Lockman, *D and D_s production in the range $3.8 GeV \leq \sqrt{s} < 4.5 GeV$*, SLAC Memorandum to the Mark III Collaboration, March 30, 1987.

[14] For an excellent review of D_s decays, see, for example: R. Rückl, *Weak Decays of Heavy Flavours*, Habilitationsschrift submitted to the University of Munich, October 1983.

[15] M. Bauer, B. Stech, M. Wirbel, Z. Physik **C 34**, 103 (1987)

[16] I.I Bigi, *On Charm Decays – Present Status and Future Goals* SLAC - PUB - 4349, june 1987

[17] Mark III Collaboration, R. Schindler, *New Results on Charmed D-meson decay*, SLAC - PUB - 3799 (1985)

[18] M. Derrick *et al.*, Phys. Rev. Lett. **54**, 2568 (1985)

[19] W. Braunschweig *et al.*, Z. Phys. **C 35**, 317 (1987)

[20] W.Y. Chen *et al.*, Phys. Lett. **B 226**, 192 (1989)

[21] M.P. Alvarez *et al.*, Phys. Lett. **B 246**, 192 (1990)

[22] F. Butler *et al.*, Phys. Lett. **B 324**, 255 (1994)

[23] H. Albrecht *et al.*, Phys. Lett. **B 255**, 634 (1991)

[24] P.L. Frabetti *et al.*, Phys. Lett. **B 313**, 253 (1993)

[25] F. Muheim, S. Stone, Phys. Rev. **D 49**, 3767 (1994)

[26] J. Adler *et al.*, Phys. Rev. Lett. **64**, 169 (1990)

[27] J.Z. Bai *et al.*, Nucl. Instr. Meth. **A 344** 319 (1994)

[28] F. Grancagnolo, *Observation of the decay $J/\psi \rightarrow \gamma\eta(c)$*, etc. Ph.D. thesis, p. 83 (1983)

[29] J. VaVra *et al.*, Nucl. Instr. Meth. **203**, 109 (1982)

[30] Private communication by Chen ShaoMin, 4/1995.

[31] T. Sjöstrand, Comput. Phys. Commun. **39**, 347 (1986)

[32] Suh Urk Chung, *Spin Formalisms*, Lectures given in the Academic Training Program of CERN, 1969-70

[33] M. E. Rose, *Elementary Theory of Angular Momentum*, Chapter IV; John Wiley & Sons, 1957

[34] E. P. Wigner, *Group Theory and its Applications to the Quantum Mechanics of Atomic Spectra*; Academic Press, 1959

[35] Particle Data Group, Phys. Rev **D 50**, *Review of Particle Properties*